UiT
THE ARCTIC
UNIVERSITY
OF NORWAY

Faculty of Science and Technology
Department of Physics and Technology

The influence of mass loss on the dynamics of dust near the Sun

Kassi Klepper

Master thesis in space physics, FYS-3931 - December 2021

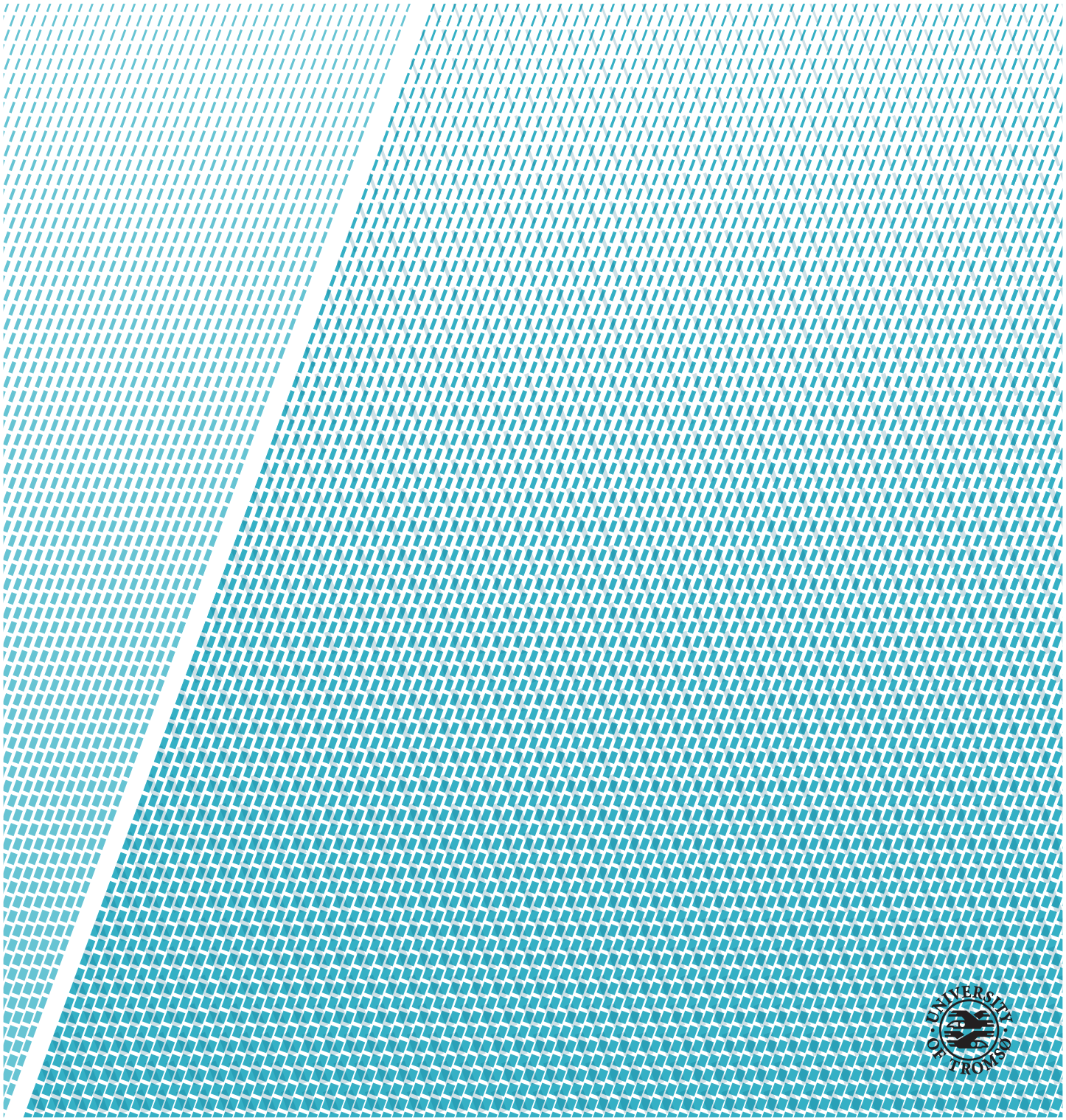

Abstract

The Parker Solar Probe (PSP) mission by NASA and the Solar Orbiter (SolO) mission by ESA are two recently launched missions that measure dust in the inner solar system. The dust is produced by fragmentation of meteoroids, which are large fragments of the asteroids and comets. The dust particles are small enough that their motion is affected by the radiation pressure force from the Sun. Dust fragments that are ejected from the solar system by this force are referred to as β-meteoroids, and initial data analysis shows that their impacts are measured by the PSP and SolO spacecraft (Szalay et al. (2020), Zaslavsky et al. (2021)). In the harsh space environment of the inner solar system, the dust grains may experience mass loss along their trajectories due to sublimation, sputtering and collisions with other dust grains. This thesis investigates the influence of the mass loss on the dynamics of dust in the inner solar system, in view of the PSP and SolO missions. The dust sizes at which the sputtering process is of importance is identified, and orbital calculations are performed to evaluate the effect of sputtering on the orbits of dust with low and high eccentricities. The dust in the inner solar system that is measured by PSP and SolO is so far assumed to be either dust in near circular, bound orbits or β-meteoroids. Based on the calculations performed in this thesis, a third dust component is predicted. This is dust in highly elliptical orbits that are significantly affected by sputtering. It is likely that the ongoing missions may identify this component, and so it is proposed for future work to calculate in detail the flux rate of these dust grains onto the PSP and SolO. The presented calculations show that in general the sputtering is an important process of mass loss for dust at distances between 0.1 and 1 AU from the Sun and that this mass loss changes perihelia and aphelia of the dust orbits. The influence of sputtering on the mass of β-meteoroids is however small and it is reasonable to assume that β-meteoroids have a constant mass.

Acknowledgements

I would like to thank my supervisor, Professor Ingrid Mann, for many years of guidance and for supporting me throughout my thesis work. Our discussions are always enlightening and inspiring. Thank you also to Dr Audun Theodorsen and to Samuel Kočiščák for helpful comments and discussions, and for sharing your experience. Thank you to the space physics group for being such an open community, and for always answering my many questions.

I am thankful for having had the most supportive and encouraging students and friends by my side all these years, this would not have been the same without you. Lastly, thank you to my family and to my people in Tromsø, for believing in me and for reminding me of and enriching my life outside of university. I appreciate you all, and I look forward to all that is yet to come.

Contents

List of Figures

List of Tables

1 Introduction

Small objects like asteroids and comets are present in our solar system, and can fragment into very small particles, for example due to collisions. These fragments are meteoroids and dust particles, and they are distributed throughout most of the solar system. The smaller fragments, typically with radii around 100 micrometer and below are referred to as dust particles. They are more abundant and form the interplanetary dust cloud. This dust cloud has been investigated remotely by researchers through observations of the zodiacal light and the F-corona (Mann et al., 2004). Recently, two space missions were launched providing in situ measurements of the dust in the inner solar system as well. These are the Parker Solar Probe (PSP) mission by NASA (Fox et al., 2016) and the Solar Orbiter (SolO) mission by ESA (Mueller et al., 2013), launched in 2018 and 2020, respectively. The PSP satellite measures dust impacts at distances closer to the Sun than any space mission has thus far, providing opportunities to better understand the properties of dust near the Sun.

The PSP and SolO satellites perform their observations in a space environment heavily affected by a high temperature and the solar wind. Dust subjected to these harsh conditions may experience a mass loss due to processes like sublimation and sputtering (Baumann et al., 2020). The dust can also be destroyed by collisions with other dust particles, which becomes more likely in the inner solar system because the dust density increases towards the Sun (Grün et al., 1985). Because of their small size, the motion of the dust particles is affected by the solar radiation pressure force in addition to the gravitational pull from the Sun. The ratio of these two forces is referred to as the β-value of

the dust. For dust particles of the same material, this parameter varies with the mass of the dust. Thus, mass loss along the dust trajectory changes the β-value of the dust, and may therefore also affect the dust trajectory. As a result of mass loss, some dust grains are therefore ejected from the solar system by the radiation pressure force, and these are called β-meteoroids.

This thesis investigates how the dust dynamics near the Sun is influenced by mass loss due to sublimation and sputtering, and addresses the significance of these processes in view of the PSP and SolO missions. Chapter 2 in this thesis introduces how the radiation pressure force to gravity force ratio is used to describe the motion of dust, and provides a general background on β-meteoroids. Some background on how the PSP and SolO satellites measure the dust is presented as well, and three mass loss process are described; sublimation, sputtering and collisions. The implementation of orbital calculations accounting for mass loss is presented in Chapter 3, including the models and expressions used for the dust dynamics and mass loss processes. The resulting mass loss rates and corresponding dust lifetimes are presented and discussed in Chapter 4, along with the resulting orbits. Finally, Chapter 5 concludes the thesis and discusses future work. A summary of the constant parameters used throughout the calculations is provided in Appendix A, and additional results that are not included in the text are presented in Appendix B. The code written to perform the calculations for this thesis work is provided in Appendix C.

2

Background

This chapter provides a background for description of the motion of dust in orbits around the Sun, particularly in the inner solar system. Section 2.1 discusses the nature of dust orbits in terms of the β-value. Further, there are currently two satellite missions measuring dust in this region, PSP by NASA and SolO by ESA, and the dust measurements are described in Section 2.2. Initial results from these missions provide knowledge about the spatial distribution of the dust number density, and this is summarized and compared to previous models in Section 2.3. Further, three different mass loss processes relevant for dust near the Sun is discussed in Section 2.4; sublimation, sputtering and collisions. Finally, the research questions addressed in this thesis are discussed in Section 2.5.

2.1 Dust in bound and unbound orbits

The dust in the solar system is mainly assumed to be produced by fragmentation of larger objects, such as asteroids or comets. These are referred to as the parent objects of the dust. Due to their size, their trajectories are governed by the gravitational pull from the Sun, or other large objects. As they collide and fragment however, dust grains of much smaller sizes are produced, and these can be affected by both the solar wind and the Sun's magnetic field as well (Mann et al., 2004). When the charge to mass ratio of the dust is very low, the Lorentz force can be neglected, and the motion of the dust can generally

be described by the solar radiation pressure force and the gravity force from the Sun. Thus, since these are both radial forces, the ratio between them is a useful term in describing the dust trajectories. This is typically referred to as the β-value of the dust grain, and is expressed below.

$$\beta = \frac{F_{rad}}{F_g} \tag{2.1}$$

It becomes apparent from the equation of motion, derived and explained in Chapter 3, that the β-value determines the nature of the dust orbit.

In the following discussion, dust grains that are released from parent objects in bound, circular orbits are considered. From Equation 2.1, it is clear that $\beta = 0$ corresponds to a case where the radiation pressure force is zero, and gravity is the only force working on the dust. This therefore describes dust grains in bound, circular orbits. Increasing the radiation pressure force results in a non-zero β-value, which increases the initially negative acceleration of the grains. The resulting magnitude of the acceleration depends on the β-value, and four cases are discussed here. For $0 < \beta < 0.5$, the dust grains remain in bound orbits, but with eccentricities increasing with the radiation pressure force. These orbits are therefore elliptical. For $\beta > 0.5$, the orbits become unbound, and the dust is ejected from the solar system in hyperbolic orbits. When $\beta = 1$, the radiation pressure force cancels out the gravity force, resulting in zero acceleration and dust grains exiting the solar system with constant velocities. Finally, for $\beta > 1$, the dust accelerates in trajectories away from the Sun with increasing velocities. This description of dust orbits in terms of β is summarized below and is valid for dust particles initially in bound, circular orbits.

- $\beta = 0$, bound, circular orbits
- $0 < \beta < 0.5$, bound, elliptical orbits
- $\beta \geq 0.5$, unbound, hyperbolic orbits

The dust grains in unbound orbits, with $\beta \geq 0.5$, are ejected and therefore contribute to loss of material in the solar system. These are called β-meteoroids.

The radiation pressure force to gravity force ratio, as discussed above, affects the motion of the dust. These forces are discussed in further detail in Chapter 3. For now, however, it is sufficient to note that they scale equally with distance from the Sun, and so the ratio does not vary with distance. Additionally, both forces depend on either the size or mass of the dust, which introduces a mass dependency on β. Near the Sun, there are several processes that can result in dust grains losing mass, and these processes are therefore also altering the

β-value of the grains. These mass loss processes may therefore play a role in the dynamics of dust near the Sun.

2.2 Dust detection with antenna measurements

There are two satellite missions measuring dust impacts in the inner solar system today. These are the PSP mission by NASA (see for example Fox et al. (2016)) and the SolO mission by ESA (see for example Mueller et al. (2013)). The PSP mission was launched in 2018 and is currently in it's tenth orbit with a perihelion at ~0.062 AU, per December 2021. By the satellite's end of life, it is scheduled to have completed 24 revolutions around the Sun, divided into seven orbit families. These are all in the solar equatorial plane, but have different perihelion distances. At its closest, the PSP satellite will be at a distance of ~0.046 AU from the Sun (Szalay et al., 2020). The current perihelion of PSP is already the closest to the Sun a satellite has ever been, and the ongoing in situ observations therefore provide an opportunity to further develop models for dust in the innermost part of the solar system. The SolO mission was launched in 2020, and completed its initial cruise phase in November 2021. The closest scheduled perihelion is ~0.28 AU, meaning it will not come as close to the Sun as PSP. However, the orbits of the SolO spacecraft will have varying inclinations relative to the solar equatorial plane, up to 33° (Mueller et al., 2013). The observations from SolO can therefore provide valuable insight into the dust properties at higher latitudes.

The primary scientific objectives of these two missions are related to heating of the solar corona and drivers of the solar wind. Thus, there are no dedicated instruments for dust measurements on either satellite. It is however, possible to detect an impact of a dust grain onto the spacecraft by a signature change in the electric potential. When a dust grain collides with the spacecraft material, it can create a momentary cloud of charges around the spacecraft. This results in an increase or decrease of the spacecraft potential, depending on its initial floating potential, and the signal is often recognized as a pulse shape. The properties of the signal shape, such as the amplitude and timescales of different parts of the pulse, is then used to derive properties of the impacting dust grain (Mann et al., 2019). Another interesting parameter available from the in situ measurements is the rate at which dust impacts occur. This depends on the area of the spacecraft, and on the spatial density distribution and impact speed of the dust (Szalay et al., 2020).

$$R = A_{sc} n v_{imp} \tag{2.2}$$

Here, R is the impact rate, A_{sc} is the area of the spacecraft that is subjected to impacts, n is the spatial density of the dust and v_{imp} is the dust impact

speed. When A_{sc} is known from satellite specifications and R is derived from antenna measurements, one can use models for impact speed and investigate the spatial density distribution of the impacting dust. This is done by Szalay et al. (2020) using data from the second orbit of PSP, and this is discussed in further detail Section 2.3. They show that the measured dust impact rate onto PSP is best described using a density profile corresponding to one of β-meteoroids, rather than dust in circular, bound orbits. Zaslavsky et al. (2021) show that the measurements of dust impacts onto the SolO spacecraft is consistent with impacts from β-meteoroids as well, derived from the velocity components of the impacting dust.

As previously mentioned, β-meteoroids are a sink of material in the solar system. An estimate for the amount of material exiting the solar system per day can thus be derived from the flux of β-meteoroids (Szalay et al., 2020). As the initial measurements from PSP and SolO both suggest that the impacting dust are β-meteoroids, investigating the dynamics of dust in the regions around the orbital distances of the satellites is of interest to support the development of models derived from the satellite data.

2.3 Density profiles of dust in the solar system

The spatial density distribution of the dust cloud in the solar system varies with distance from the Sun. A general understanding is that the density increases with decreasing distance, and so the dependency follows some inverse power law.

$$n(r) \sim r^{-\nu} \tag{2.3}$$

Here, n is the spatial density distribution as function of distance from the Sun r. The exponent ν of this general relation has been investigated both analytically and by observations. Grün et al. (1985) show that under ideal conditions of dust in circular orbits, the exponent is $\nu = 1$. However, using zodiacal light measurements from space missions Helios 1 and 2, it is found to be $\nu = 1.3$ between 0.3 AU and 1 AU (Leinert et al., 1981).

$$n_c(r) \sim r^{-1.3} \tag{2.4}$$

While this suggest that there is a deviation from the ideal case, the subscript c for circular orbits is added for simplification.

Szalay et al. (2020) derive a density model for β-meteoroids from the vis-viva equation and conservation of mass, which is valid at a sufficiently large distance from where the dust was formed.

$$n_\beta(r) \sim r^{-2} \tag{2.5}$$

The subscript β denotes that the model is valid for β-meteoroids. The range of β-values for which this model applies depends on the source region of the dust. In their discussion, the source region is defined at $5R_{\odot}$, solar radii, which approximates to 0.02 AU, yielding a range of β-values between 0.6 and 1.2. This density model for β-meteoroids is further compared to the density model $n_c(r)$ in the following manner.

As discussed in Section 2.2, the measured impact rates R of dust onto the PSP and SolO satellites depend on the density profile, shown in Equation 2.2. The impact rate is proportional to the product of dust impact speed and density, and so the expected impact rate of circular, bound dust R_c is estimated using values from circular dust models. Similarly, the expected impact rate of β-meteoroids R_β is estimated using values from β-meteoroid models.

$$\begin{aligned} R_c(r) &\propto v_{imp,c}(r) \cdot n_c(r) \\ R_\beta(r) &\propto v_{imp,\beta}(r) \cdot n_\beta(r) \end{aligned} \tag{2.6}$$

In Figure 7 in their paper, Szalay et al. (2020) compare the measured impact rate onto PSP in its second orbit, and show that the measurements best coincide with R_β. This suggests that the dust measured by PSP is β-meteoroids.

2.4 Mass loss processes

New in situ measurements from the PSP and SolO missions show that the measured dust impacts most likely are caused by β-meteoroids ejected from the solar system. If a dust grain loses mass along its trajectory, the β-value will change due to its mass dependency and the dust trajectory is altered as well. In order to better describe the dust dynamics, a potential mass loss should be accounted for in the orbital calculations. Here, three mass loss processes relevant in regions near the Sun are considered; sublimation, sputtering and collisions with other dust particles.

2.4.1 Sublimation

Sublimation is a process where solid material is transformed to gaseous material due to high temperatures. This happens without the material entering the liquid phase. Baumann et al. (2020) calculates the sublimation mass loss rate from Langmuir's equation of evaporation, given below. However, in their paper, the parameter A_s (A in their paper) is included in the square root. This does not give the correct unit of the mass loss rate, g/s, and reproducing their results verifies that they have implemented the expression below in their calculations,

and that the mistake in the paper is simply a misprint.

$$\frac{dm_{sub}}{dt} = -p_v(T)A_s\sqrt{\frac{M}{2\pi RT(r)}} \tag{2.7}$$

Here, M is the mean molecular mass of the dust material, A_s is the entire surface area of the dust and R is the universal gas constant. $T(r)$ is the dust temperature as function of the distance from the Sun, while $p_v(T)$ is the vapor pressure as function of the dust temperature. These are discussed further in Chapter 3.

As can be seen in Equation 2.7, the sublimation mass loss rate is strongly dependent on the distance. Mann et al. (2004) discuss several estimates of the sublimation zone, in other words the region where different dust materials sublimate, presented in their Table 2. With one exception for some magnetite particles calculated by Mukai and Schwehm (1981), the estimates give sublimation zones within 0.1 AU. The sublimation lifetimes calculated in Baumann et al. (2020) agree with the estimates as well.

2.4.2 Sputtering

Behrisch and Eckstein (2007) define sputtering as "the physical process of atom ejection from a solid through the bombardment of energetic ions". This process can happen when the dust interacts with the solar wind, being hit by its energetic ions. The process depends on both the energy and composition of the solar wind ions and on the dust material, and the sputtering mass loss rate can be expressed as follows (Baumann et al., 2020).

$$\frac{dm_{sput}}{dt} = -f_{SW}Y_{tot}Am_A \tag{2.8}$$

The parameter m_A is the mean atomic mass of the sputtered atoms and A is the geometric cross section of the dust. These parameters thus include the dependence on the dust properties. Further, f_{SW} is the solar wind flux, which includes the dependency on energy of the impacting ions. It is the product of the plasma density and speed of the solar wind, and the latter varies with solar wind conditions (Baumann et al., 2020). For example, the solar wind speed increases during a coronal mass ejection (CME) event, compared to slow solar wind speed, and the flux thus increases as well (Mann et al., 2004). From Equation 2.8, this results in an increased absolute sputtering mass loss rate during the CME event. Finally, Y_{tot} is the total sputtering yield. This can be seen as a sputtering efficiency factor, and the solar wind composition dependency is included in this term. The sputtering yield is derived and further discussed in Chapter 3.

2.4.3 Collisions

While the discussion of dust trajectories thus far has been regarding single particle motion, it is important to keep in mind that a significant mass loss process in the solar system is collisions with other dust grains (Mann et al., 2004). Grün et al. (1985) consider catastrophic collisions, meaning that the dust is completely destroyed in a single collision event. This is unlike sublimation and sputtering, where the dust material erodes over time. To compare the three processes, it is therefore helpful to evaluate the dust lifetimes, that is, how long the dust survives before it is destroyed by either process. The collision lifetime is dependent on the properties of the evaluated dust grain, and on the dust size- and density distribution in the solar system. This is further discussed and derived in Chapter 3.

2.5 Research questions

The dominant mass loss process for dust at distances closer to the Sun than 0.1 AU is commonly considered to be sublimation. Its influence on the dynamics has been studied in a number of works, see Mann et al. (2004) and references therein. Outside of 0.1 AU however, the dust may be destroyed by mass loss due to sputtering, and by a collision with another grain. This thesis addresses the question of which of these processes can be considered dominant for dust between 0.1 AU and 1 AU. Additionally, since these processes both depend on dust size and distance from the Sun, whether there is a critical size or distance where the dominant mass loss process changes from one process to the other is investigated.

The mass loss that results from sputtering influences the dynamics of the dust because the β-value is a function of mass and this work investigates whether this influence is significant. An open questions is whether the sputtering can lead to to production of β-meteoroids, meaning that a dust grain initially in a bound orbit can be ejected as a result of the sputtering mass loss. Another open questions is whether the sputtering can significantly reduce the size of the ejected β-meteoroids. Another open question is how the trajectories of dust grains change as a result of the sputtering. These open questions are addressed in the orbital calculations performed for this thesis.

3 Method

Dust in the inner solar system may lose mass because of sublimation, sputtering and collisions, and for small dust grains, the resulting mass loss can affect the orbit of the dust. This chapter presents a way to calculate the dust trajectories, accounting for mass loss along the orbits.

3.1 Mass loss rates

This section describes how the mass loss rates of sublimation and sputtering presented by Baumann et al. (2020) are calculated, and derives any necessary parameters. Estimates used in the calculations are also presented here. Further, the collision lifetimes presented by Grün et al. (1985) are derived and scaled to be a function distance and dust size.

3.1.1 Sublimation

Baumann et al. (2020) use the Langmuir's equation of evaporation to calculate the sublimation mass loss rate, provided here in Equation 2.7. The mean molecular mass M in the equation depends on the type of dust material, and three materials are considered in their paper; $Fe_{0.4}Mg_{0.6}O$ (henceforth referred to as metal oxide dust for simplicity), silicate dust and carbon dust. The values used for this parameter is included in Table A.1. Next, the parameter A_s is

the surface area of the dust grain. Here, a spherical geometry of the dust is assumed, meaning $A_s = 4\pi r_d^2$. The dust radius r_d is assumed to change with the mass following a homogeneous distribution of mass within the dust grain, and is therefore not a constant in these calculations. The dust temperature $T(r)$ varies with distance from the Sun r, and the vapor pressure $p_v(T)$ is a function of the dust temperature. Both of these parameters are discussed in detail below.

The mass loss rate due to sublimation is as described above a function of both distance from the Sun and dust size. The sublimation lifetime for a given mass subjected to the mass loss rate in Equation 2.7 at a given distance is then calculated by:

$$\tau_{sub}(r, r_d) = \frac{m}{dm_{sub}/dt} \tag{3.1}$$

Dust temperature

The dust temperature for dust with radius 1 nm, 5 nm and 20 nm is provided in the supplemented material of Baumann et al. (2020), for three dust materials; metal oxide, silicate and carbon dust. Myrvang (2018) calculates the dust temperature for a range of sizes and materials, and shows in the Appendix that dust of similar materials with a radius of 1 μm follows a blackbody temperature curve, $T_{bb}(r)$. This approximation assumes that all of the absorbed power is emitted from the grain, expressed below.

$$F_\odot(r)A = \sigma T_{bb}(r)^4 A_s \tag{3.2}$$

Here, $F_\odot(r)$ is the flux from the Sun onto a grain with cross section $A = \pi r_d^2$ for spherical dust. The surface area of the grain $A_s = 4\pi r_d^2$, and σ is the Stefan-Boltzmann constant. The flux at 1 AU is known as the solar constant, and this is used as a reference value to scale the flux with distance.

$$F_\odot(r) = F_{\odot,0}(r_0)\left(\frac{r_0}{r}\right)^2 \tag{3.3}$$

The solar constant $F_{\odot,0}(r_0 = 1 \text{ AU}) = 1361 \text{ W/m}^2$ (Schmutz et al., 2013). Inserting this relation into Equation 3.2 and solving for $T_{bb}(r)$ yields the following expression.

$$T_{bb}(r)^4 = \frac{F\pi r_d^2}{4\pi r_d^2 \sigma} = \frac{F}{4\sigma} = \frac{F_0(r_0) r_0^2}{4\sigma}\frac{1}{r^2}$$

$$T_{bb}(r) = \left(\frac{F_0(r_0) r_0^2}{4\sigma}\right)^{1/4} \frac{1}{\sqrt{r}} \tag{3.4}$$

The data provided by Baumann et al. (2020) and the calculations for nanometer sized dust in Myrvang (2018) both show that smaller particles deviate from the blackbody temperature curve. This suggests that the blackbody approximation derived above best works for micrometer sized dust, and that a correction should be implemented in the calculations for smaller particles. Figure 3.1 shows the deviation between the data provided in the supplemented material in Baumann et al. (2020) and the blackbody temperature approximation, for two nanometer sized dust grains. It shows that the approximation is best for silicate dust, and that the deviation is lower at larger distances for all materials.

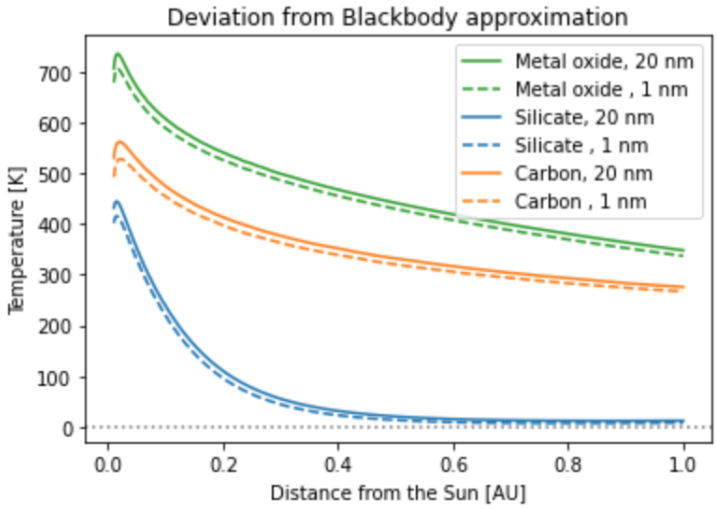

Figure 3.1: Temperature deviation between data provided in the Baumann et al. (2020) supplemented material and the blackbody approximation. Plotted for three materials, for two dust radii of 1 nm and 20 nm.

In the sublimation mass loss rate and lifetime calculations performed here, the approximation is applied to micrometer sized dust. For nanometer sized dust, the blackbody temperature is corrected to fit the temperature data provided by Baumann et al. (2020). It should be noted that the temperature is a function of dust size as well as of distance, and the provided data is for 1 nm, 5 nm and 20 nm only. The temperature is therefore interpolated for dust sizes within this range of dust radii.

Vapor pressure

The vapor pressure is a function of the dust temperature and the material of the dust. It is however, independent of dust size as presented in the data by Baumann et al. (2020). Thus, to obtain a value for the vapor pressure for a

given material at a given distance, the following algorithm is performed. First, the distance dependent temperature is determined as discussed above. Next, all temperature data points within a dust species are combined and sorted in a rising order, that is for all three dust sizes and all distances. The vapor pressure data is sorted accordingly, and an interpolated function is created from the sorted temperature and vapor pressure data.

An apparent limitation to using the data provided by Baumann et al. (2020) to calculate the temperature and vapor pressure is the range of the provided data. The temperatures with corresponding vapor pressure values are given for distances between 0.01 AU and 1 AU, for three dust sizes and three dust materials. The size limitation affects the temperature calculations, and for dust outside of the data range, a blackbody approximation is used instead. The distance range covers the main region of interest in this project, including the distances where the new measurements from the PSP and SolO missions are acquired. Thus for the purpose of this project, these ranges suffice, and so the method is considered an adequate approach.

3.1.2 Sputtering

The mass loss rate due to sputtering is given in Equation 2.8, and depends on properties of both the dust and the solar wind. The mean atomic mass m_A depends on the dust material, and the values used in these calculations are provided in Table A.1. The geometric cross section of the dust A is calculated assuming a spherical grain, such that $A = \pi r_d^2$. The mass loss rate also depends on the solar wind flux f_{SW} and the total sputtering yield Y_{tot}, both of which are discussed below.

The time it takes for the dust particle to be destroyed by the sputtering mass loss process is referred to as the sputtering lifetime, τ_{sput}. Applying the calculated sputtering mass loss rate to a dust grain with a given mass at a given distance, thus results in the following lifetime:

$$\tau_{sput}(r, r_d) = \frac{m}{dm_{sput}/dt} \tag{3.5}$$

Solar wind flux

The flux of solar wind ions can be expressed as the product between the plasma density n_p and the solar wind speed v_p (Baumann et al., 2020).

$$f_{SW} = n_p v_p \tag{3.6}$$

The solar wind speed can be considered constant with distance from the Sun in the inner solar system. It does however, depend on the inclination of the dust orbit, and is normally categorized as either slow or fast solar wind. A dust grain orbiting in the solar equatorial plane is subjected to slow solar wind, while dust at higher solar latitudes experiences fast solar wind (Mann et al., 2010). Additionally, CME events can increase the solar wind speed for the duration of the event, thus increasing the solar wind flux as well. Baumann et al. (2020) estimate the slow solar wind speed to be 300 km/s and the CME wind speed to be 500 km/s.

The plasma density is a function of the distance from the Sun, and Venzmer and Bothmer (2018) estimate it to scale as approximately r^{-2}. Using a known reference value then provides a scaled model for the plasma density as expressed below.

$$n_p(r) \sim n_{p,0}(r_0) \left(\frac{r_0}{r}\right)^2 \tag{3.7}$$

Here, an estimate of $n_{p,0}(r_0 = 0.16\,\text{AU}) = 214\,\text{cm}^{-3}$ is used (Venzmer and Bothmer (2018)). The solar wind flux is therefore a function that scales with distance as r^{-2} as well.

Sputtering yield

The sputtering yield can be interpreted as an efficiency factor of the sputtering process, describing how many atoms are ejected from the dust surface by an incident ion (Baumann et al., 2020). The solar wind is composed of several types of ions, interacting with the dust material during the sputtering process. To calculate the total sputtering yield for a given solar wind composition and a given dust composition, one first have to consider how efficiently each of the solar wind ion types sputters the dust material. The following indices are used throughout the derivation:

- j: Dust component, e.g. for silicate dust: Mg, Fe, Si or O
- k: Solar wind ion: H, He, C, O, N, Fe, Ne, Mg, Si or S

The specific sputtering yield of a solar wind ion k onto all dust components j can be expressed as:

$$Y_k = \sum_j Y_{j,k} \tag{3.8}$$

For example, if k corresponds to helium, and we consider silicate dust, Equation 3.8 gives us the following specific sputtering yield.

$$Y_{He} = Y_{He\to Mg} + Y_{He\to Fe} + Y_{He\to Si} + Y_{He\to O}$$

The notation $Y_{k\to j}$ denotes the sputtering yield of solar wind ion k onto dust component j. These values are provided in the supplemented material of Baumann et al. (2020). The total sputtering yield is then calculated by adding the specific yields of all solar wind ions, weighted by their abundance in the solar wind.

$$Y_{tot} = \sum_k c_k Y_k \tag{3.9}$$

Here, c_k is the abundance of the solar wind ion k, which varies with solar wind conditions. Killen et al. (2012) provide the solar wind ion abundance for several conditions in their Table 6, and the abundances for slow solar wind and CME conditions are plotted below for illustration.

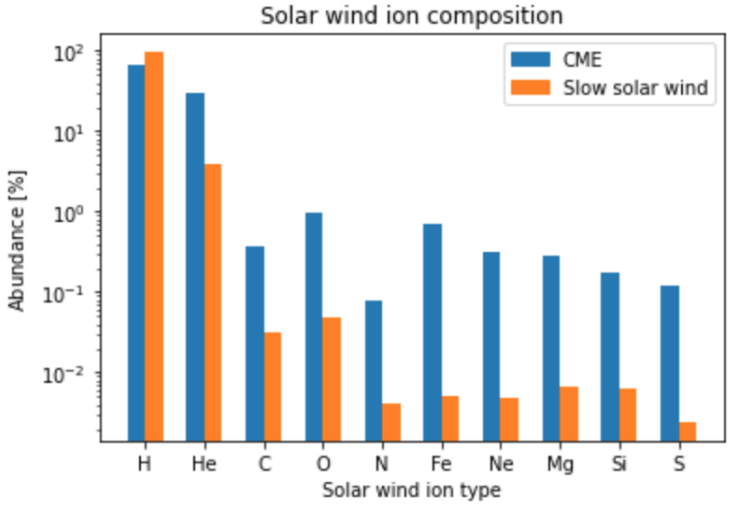

Figure 3.2: Solar wind ion composition, values from Killen et al. (2012).

As shown in Figure 3.2, there is a higher abundance of heavier elements during a CME event, than there is in the slow solar wind.

Equation 2.8 and the above discussion show that the sputtering mass loss rate is a function of the size of the dust, and the distance from the Sun. The dependence on the solar wind conditions is shown in Equations 3.6 and 3.9. For example, the speed of the solar wind ions v_p increases during a CME event, which in turns increases the solar wind flux. Additionally, when the abundance of heavy ions in the solar wind increases, altering the c_k parameter, the total sputtering yield changes as well. In order to investigate how significant a variation in the solar wind condition is to the sputtering mass loss rate, the implementation includes both calculations for slow solar wind and CME events.

3.1.3 Collisions

The collision lifetime τ_c describes how long a dust grain with mass m can exist in an orbit at distance r before it collides with another particle. As previously mentioned, a collision is considered fatal to the dust grain. The lifetime is the inverse of the collision rate c, which depends on the properties of the dust grain itself and on the distribution of dust in the solar system.

$$\tau_c(r, m) = \frac{1}{c(m, r)} \propto \frac{1}{\sigma(m) F(m, r)} \tag{3.10}$$

The collision rate c is proportional to the product of the collision cross section $\sigma(m)$ and the flux $F(m, r)$ of colliding dust (Grün et al., 1985). In the model presented by Grün et al. (1985), the collision cross section is simplified to the geometric cross section. As a result of this approximation, the collision cross section depends on the mass of the dust grain and on the size distribution of the dust in the solar system. Zodiacal light observations suggest a constant size distribution with distance from the Sun (Mann et al., 2004), and so the collision cross section is independent of distance. This means that the collision lifetime scales as the inverse of the particle flux with distance. In this section, the distance dependency of the particle flux is derived based on the models used in Grün et al. (1985). They present estimates of the collision lifetime for a range of dust masses for two distances, at $r = 0.1$ AU and $r = 1$ AU. Using these estimates as reference values, the collision lifetime is scaled with distance as the inverse of the particle flux, to implement the distance dependency of the collision lifetime. This derivation from Grün et al. (1985) is included below, as it may not be obvious at first read through of the text.

Assuming a constant dust size distribution, the particle flux F can be expressed as below.

$$F(m, r) = \frac{1}{k} \overline{v}(r) n(m, r) \tag{3.11}$$

Here, $\overline{v}(r)$ is the average impact speed of the dust at a distance r from the Sun, and $n(m, r)$ is the number density of dust with mass m at distance r. The parameter k is a constant that depends on the dust geometry and the directionality of the flux. If the average impact speed scales with distance as a particle with circular velocity, the term $\overline{v}(r)$ can be re-written as the following expression.

$$\overline{v}(r) = \overline{v}_0(r_0) \left(\frac{r}{r_0} \right)^{-0.5} \tag{3.12}$$

The parameters $\overline{v}_0$ and r_0 are reference values. Grün et al. (1985) estimate $\overline{v}_0(r_0 = 1 \text{ AU}) = 20$ km/s. The high estimate of the impact speed suggests an inclination between the colliding dust orbits, or that their orbits have different eccentricities.

Grün et al. (1985) assume a cylindrical symmetric dust cloud, and therefore only consider a distance dependency of the density. They assume a density model equal to $n_c(r)$, previously presented in Section 2.3, Equation 2.4.

$$n(r) = n_c(r) \sim r^{-1.3} \tag{3.13}$$

Scaling the number density using known reference values therefore results in the following expression.

$$n(m, r) = n_0(m, r_0) \left(\frac{r}{r_0} \right)^{-1.3} \tag{3.14}$$

Combining Equations 3.11, 3.12 and 3.14 to obtain a scaled function of $F(m, r)$ yields the following derivation.

$$\frac{F(m,r)}{F_0(m,r_0)} = \frac{1/k}{1/k} \frac{\overline{v}(r)}{\overline{v}_0(r_0)} \frac{n(m,r)}{n_0(m,r_0)} = \left(\frac{r}{r_0} \right)^{-0.5} \left(\frac{r}{r_0} \right)^{-1.3} = \left(\frac{r}{r_0} \right)^{-1.8}$$

$$\Rightarrow \qquad F(m,r) = F_0(m,r_0) \left(\frac{r}{r_0} \right)^{-1.8} \tag{3.15}$$

Finally, since the collision lifetime scales as the inverse particle flux with distance, the collision lifetime as function of both distance and mass can be expressed as follows.

$$\tau_c(r, m) = \tau_{c,0}(r_0, m) \left(\frac{r}{r_0} \right)^{1.8} \tag{3.16}$$

In Figure 6 in Grün et al. (1985), estimates for the collision lifetime for dust with masses between 10^{-18} g and 10^{2} g are plotted. Here, the estimates at $r = 1$ AU for an interplanetary flux model are used as the reference value $\tau_{c,0}(r_0 = 1 \text{ AU}, m)$.

3.2 Orbital calculations

This section introduces the method used to perform the orbital calculations. Section 3.2.1 presents the initial conditions and summarizes the assumptions used to calculate the orbits, while Section 3.2.2 describes the resulting equation of motion. The numerical methods implemented to perform the calculations are presented in Section 3.2.3. Finally, Section 3.2.4 describes how the initial size of the dust is selected.

3.2.1 Initial conditions and assumptions

The following calculations assume a single, spherical dust grain orbiting the Sun in the solar equatorial plane. The dust production source is assumed to be fragmentation of a larger parent object. This is here considered to be a meteoroid in a circular orbit around the Sun. When the dust is produced, it is assumed to inherit the velocity of its parent object. This means that the initial velocity of the dust grain is the circular velocity at the distance of production. The dust composition depends on the composition of the parent object, and three materials are considered in the following calculations; metal oxide, silicate and carbon dust.

First studies of the PSP and SolO observations made so far showed that the measured fluxes can be described by dust with radius in an approximate range between 100 – 500 nm (Szalay et al. (2020), Zaslavsky et al. (2021)). For dust grains of this size, the charge-to-mass ratio is small and therefore the Lorentz force small. Another analysis of PSP observations showed no indication that the observed dust fluxes are significantly affected by the Lorentz force (Mann and Czechowski, 2021). As a first approach to investigating the effect of mass loss on the dust dynamics in view of the PSP and SolO observations, the Lorentz force is not included in the calculations. The forces working on the dust grain is thus the gravitational pull from the Sun and the solar wind radiation pressure force.

From the assumption of spherical dust geometry, it is possible to calculate the mass of a dust grain m with a given dust radius r_d, given a homogeneous mass distribution within the grain.

$$m = \rho V = \rho \frac{4\pi}{3} r_d^3 \tag{3.17}$$

The parameter ρ is the bulk density of the dust, and an estimate of 2.5 g/cm^3 is used in the calculations (Mann et al., 2004).

3.2.2 Dust dynamics

The position of objects in orbits around the Sun is often described by the orbit equation derived from Keplerian mechanics. This approach, however, assumes a constant mass, and so here a Newtonian approach is used instead to allow for mass loss along the dust trajectories. The sum of forces in the case considered here is expressed by Newton's second law as follows.

$$\sum F = ma = -F_g + F_{rad} \tag{3.18}$$

Here, m and a are the mass and acceleration of the dust grain, respectively, while F_g is the gravity force and F_{rad} is the solar wind radiation pressure force. The radiation pressure force is dependent on the size of the dust, as well as its distance from the Sun, and can be expressed as follows (Mann et al., 2004).

$$F_{rad} = L_\odot(r = 1 \text{ AU})\frac{A_s}{4\pi r^2}$$

The parameter $L_\odot$ is the solar luminosity at distance $r = 1$ AU, and A_s is the surface area of the dust grain. For a spherical dust grain, $A_s = 4\pi r_d^2$, where r_d is the radius of the dust. As discussed in Chapter 2, the beta-value of a dust grain is helpful in describing the dust motion. Remembering the parameter $\beta = F_{rad}/F_g$, presented in Equation 2.1, it can be noted that the radiation pressure term introduces a size dependency on the beta-value. From Equation 2.1, the radiation pressure force can also be expressed in terms of the gravity.

$$F_{rad} = F_g\beta, \qquad \text{where} \qquad F_g = \frac{\mu m}{r^2} \tag{3.19}$$

Here, μ is the product of the solar mass and the gravitational constant, m is the mass of the dust, and r the distance from the Sun. Thus, the beta-value also has a mass-dependency. Inserting the expressions for F_{rad} and F_g in Equation 3.19 into Equation 3.18, solving for a yields the following expression for the acceleration.

$$a = \frac{F_g}{m}(\beta - 1) = \frac{\mu}{r^2}(\beta - 1) \tag{3.20}$$

From this expression, it is possible to calculate the acceleration of a dust grain at a given distance with a given beta-value. The beta-value is a function of the dust mass, and Wilck and Mann (1996) provide beta-value estimates for different dust materials in their Table 2. Here, values for asteroidal dust is used, and an interpolated function is created from the table values. This is plotted in Figure 3.3 with the table values for illustration.

The filled, green area in Figure 3.3 highlights the mass range where $\beta > 0.5$. From the discussion in Chapter 2, dust with mass within this range can be recognized as beta-meteoroids that are ejected from the solar system. Dust with mass outside of the filled, green area are in bound orbits, because their beta-value is < 0.5.

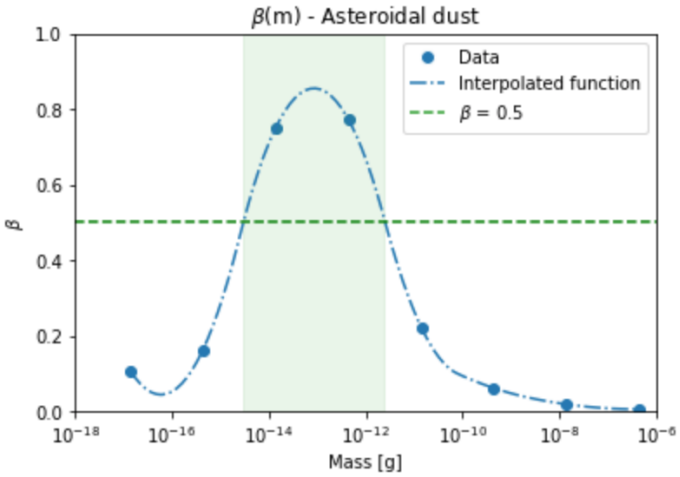

Figure 3.3: Beta as function of mass, data values from Table 2 in Wilck and Mann (1996). The green, dashed line marks $\beta = 0.5$, and the filled, green area is included to highlight the mass range where $\beta > 0.5$.

3.2.3 Numerical method

When the beta-value of the dust grain is found from the mass of the dust, using the values from Wilck and Mann (1996), and the distance is known, the acceleration of the dust grain is calculated using Equation 3.20. From this, the velocity and position is calculated using either the Euler-Cromer method or the Leapfrog integration method. Both of these are implemented for code verification and for evaluating the stability of the program.

Euler-Cromer method

The Euler method is a first-order method that uses the current acceleration a_i and velocity v_i to calculate the next velocity v_{i+1} and position r_{i+1}. Here, a Cromer modification is implemented for redundancy, meaning that the next velocity rather than the current velocity is used to calculate the next position.

$$\begin{aligned} v_{i+1} &= v_i + a_i dt \\ r_{i+1} &= r_i + v_{i+1} dt \end{aligned} \tag{3.21}$$

Leapfrog integration method

The Leapfrog integrator is a second-order method, known to perform well for large, constant time steps. The algorithm is similar to the Euler-Cromer method, but it evaluates the velocity at half-steps, and the acceleration and position at full-steps.

$$\begin{aligned} v_{i+1/2} &= v_{i-1/2} + a_i dt \\ r_{i+1} &= r_i + v_{i+1/2} dt \end{aligned} \tag{3.22}$$

3.2.4 Selecting the initial size of the evaluated dust grains

The objective of these orbital calculations is to investigate how mass loss can affect the dust trajectories. A qualitative discussion about this is possible already from Figure 3.3. In the case of mass loss, the value of the dust mass will move to the left on the ordinate axis in the figure, as the mass decreases from right to left. The change in beta-value following from this change in mass will follow the blue curve in the figure. This means that dust with an initial mass on the right hand side of the filled, green area will be in a bound orbit initially. As it loses mass, it will enter the filled, green mass range, and its orbit will become unbound. If the dust grain continues to lose mass, and reaches the left hand side of the filled, green area, its orbit would again become bound. Once the mass is on the left hand side, the dust will eventually be destroyed by the mass loss process or crash into the Sun.

This description does not consider dust lifetimes or account for varying mass loss rates, but very generally describes how dust with different initial mass behaves with mass loss. To investigate the effect of mass loss in further detail, three dust sizes are chosen for the calculations; one with initial mass on the left hand side of the filled, green area, one with initial mass within the green mass range, and one with initial mass on the right hand side:

- Dust radius $r_d = 20$ nm $\quad\longrightarrow\quad$ m $\sim 10^{-17}$ g
- Dust radius $r_d = 200$ nm $\quad\longrightarrow\quad$ m $\sim 10^{-14}$ g
- Dust radius $r_d = 2\ \mu$m $\quad\longrightarrow\quad$ m $\sim 10^{-11}$ g

3.3 Algorithm of the code written to perform the orbit calculations

The background presented in this thesis thus far is here used to calculate the orbits of dust grains experiencing mass loss along their trajectories. A program is written in Python to perform these calculations, following the algorithm presented in this Section. The code is included in Appendix C.

1. Import Python libraries
2. Define the following functions

Function name	Input(s)	Output(s)	Calculated from:
MaterialProperties	i	m_A, M	Table A.1
PlasmaDensity	r	n_p	Equation 3.7
SolarWindFlux	r, w	f_{SW}	Equation 3.6
SputteringYield	w, i	Y_{tot}	Equation 3.9
MassLossSputtering	r, r_d, w, i	dm_{sput}/dt	Equation 2.8
MassLossSublimation	r, T, p_v, r_d, i	dm_{sub}/dt	Equation 2.7
GetMass	m, r, r_d, t, w, i	m_{next}	$m_{next} = m + dm/dt$
GetBeta	m	β	Figure 3.3
GetAcceleration	β, m, r, ϕ	a	Equation 3.20
EulerCromer	r, v, ϕ, β, t	r_{next}, v_{next}, ϕ_{next}	Equation 3.21
Leapfrog	r, v, ϕ, β, t	r_{next}, v_{next}, ϕ_{next}	Equation 3.22

Table 3.1: Description of the functions implemented in the Python program written to perform the orbit calculations. The parameters i and w are iterative code parameters evaluating different materials and different solar wind conditions, respectively. The azimuth angle of the grain ϕ is used for conversion between Cartesian and polar coordinates in some sections of the code. The other parameters are described in the text.

3. Define constants and set user defined parameters
4. Calculate initial conditions from user defined parameters
5. Perform orbit calculations by repeating the following steps until a user set criterion is met
   (a) Apply mass loss and calculate resulting mass (GetMass)
   (b) Get resulting β-value (GetBeta)
   (c) Calculate current acceleration (GetAcceleration)
   (d) Calculate next position and velocity vector (EulerCromer or Leapfrog)
   (e) Calculate next angle (from trigonometry)
   (f) Store values, update current values and increment time

4

Results and analysis

This chapter presents the calculated mass loss rates and corresponding dust lifetimes in Section 4.1, as discussed in Chapter 3. Calculations determining the dominant mass loss process at different dust sizes and at distances from the Sun is included in Section 4.2. Section 4.3 verifies the program written to perform the orbital calculations. The calculated orbits of low β-value fragments are presented in Section 4.4, and sputtering as a production process of β-meteoroids is discussed here. Further, the calculated orbits for high β-value fragments are presented in Section 4.5. Sputtering as a destruction process of β-meteoroids are discussed here, as well as the influence of sputtering on fragments in highly elliptical orbits.

4.1 Mass loss rates

4.1.1 Code verification

The implemented code that calculates the mass loss rates for sublimation and sputtering is verified by using the program to calculate the lifetimes of a case presented by Baumann et al. (2020). A silicate dust grain with a radius of 1 nm under CME conditions is considered, and compared to Figure 9c in their paper.

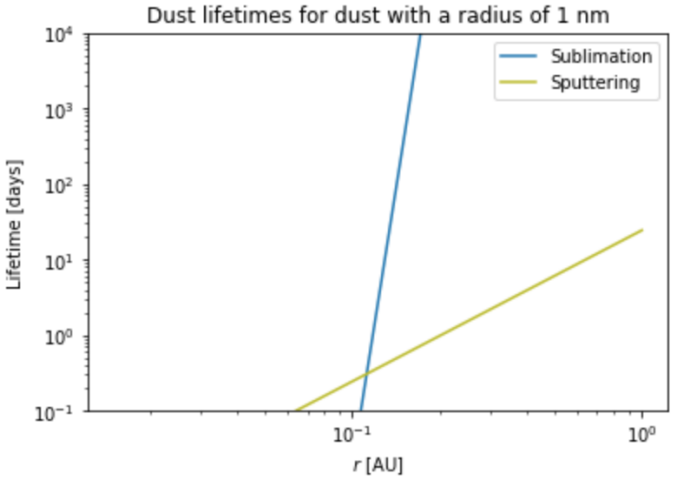

Figure 4.1: Calculated dust sputtering and sublimation lifetimes using the implemented program, for a case that is presented in Baumann et al. (2020) for code verification.

The calculated sublimation and sputtering mass loss rates and corresponding lifetimes are of the same orders of magnitude as the results presented by Baumann et al. (2020), and the slopes intersect at the same distance from the Sun, around 0.1 AU. The reproduced result verifies that the code is implemented correctly.

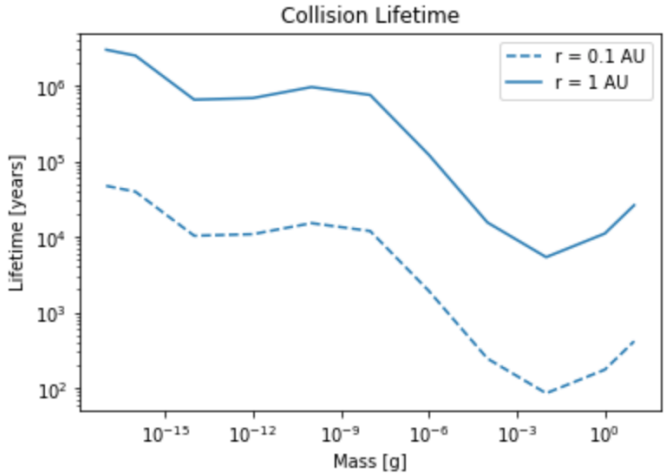

Figure 4.2: Plot of the implemented collision lifetime. The solid line is the reference values at 1 AU from Grün et al. (1985), and the dashed line is the result of using the implemented code to estimate the collision lifetimes at $r = 0.1$ AU

As described in Chapter 3, the collision lifetimes are estimated from a scaled function of a set of reference value from Grün et al. (1985). These reference values were obtained by reading off values from their Figure 6, for the interplanetary flux model at 1 AU. In the same figure, they provide estimates for 0.1 AU as well, and so the code is verified by reproducing the collision lifetimes at this distance. The results are shown in Figure 4.2, and show that the calculated collision lifetimes follow a similar curve as the estimates presented by Grün et al. (1985). While the implemented collision lifetime curve is not as smooth, this is due to the fact that the reference values were obtained from a figure. Since the resulting estimates using the code are of correct orders of magnitude, this verifies the implementation of the code.

4.1.2 Sublimation

There is general agreement that the dust sublimates inward of 0.1 AU and that there exists a dust free zone as a result of this, as discusses in Chapter 2 (Mann et al., 2004). The calculated sublimation mass loss rates performed in this thesis work agree with these estimates as well. A result of the calculated sublimation lifetimes is included in Figure 4.1. One of the results presented in Baumann et al. (2020) is reproduced for a 1 nm silicate dust grain, where the boundary of a sublimation zone can be recognized near 0.1 AU from the steep slope resulting in very low sublimation lifetimes.

Since the dust sublimates within 0.1 AU, and the sublimation lifetime is very high outside the sublimation zone, this process is regarded as the dominating mass loss process inward of 0.1 AU and its effect in considered negligible outward of 0.1 AU in the following discussion. This means that the sputtering mass loss rates and lifetimes are considered for distances larger than 0.1 AU.

4.1.3 Sputtering

Sputtering yield calculations

In order to calculate the sputtering mass loss rate, the total sputtering yield must first be evaluated. This parameter is calculated here for slow solar wind and CME conditions, for metal oxide, silicate and carbon dust. The code written to perform the calculations is included in Appendix C, and shows the implementation of Equations 3.8 and 3.9, using values for solar wind compositions from Killen et al. (2012) shown in Figure 3.2. The result is plotted in Figure 4.3, and the values are included in Table 4.1

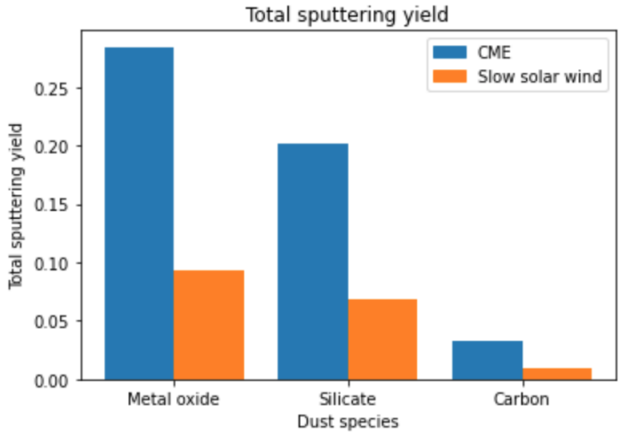

Figure 4.3: Total sputtering yield in slow solar wind and CME conditions, for metal oxide, silicate and carbon dust.

	Metal oxide dust	Silicate dust	Carbon dust
SSW	0.093675	0.068621	0.010016
CME	0.284241	0.201996	0.032754
SSW/CME	0.3296	0.3397	0.3058

Table 4.1: Calculated values for the total sputtering yield.

Figure 4.3 shows that the total sputtering yield increases during a CME event for all three materials. The sputtering yield is not a function of solar wind speed, and so this increase during CME events is due to the higher abundance of heavy elements in the solar wind. The values in Table 4.1 indicate that the increase in sputtering yield varies with materials as well, because the SSW/CME ratio is unequal for the different types of dust. This can be explained by the fact that each solar wind ion type has a specific sputtering yield for

different elements, thus also for different dust compositions. This combined effect of the dependency of solar wind composition and dust composition is part of what makes the sputtering yield such a complex parameter. In order to highlight the dependency of the solar wind composition in a clearer way, the relative sputtering yield of each solar wind ion type is plotted separately for each material. The relative sputtering yield describes how much of the total sputtering yield is caused by each ion type. By comparing this parameter for both slow solar wind and CME conditions, for each material, the effect of the higher abundance of heavy elements can be seen more easily.

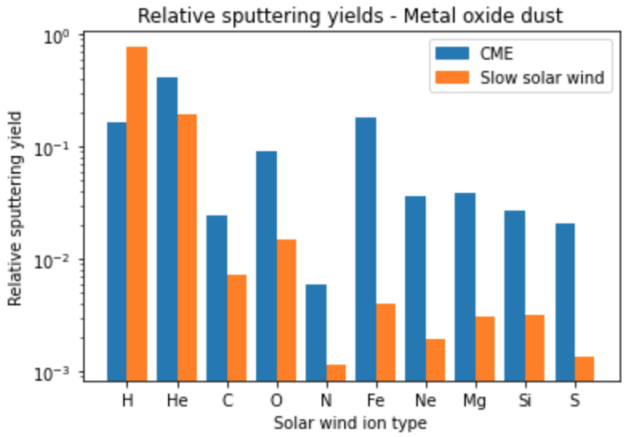

Figure 4.4: Relative sputtering yields in slow solar wind and CME conditions, for metal oxide dust.

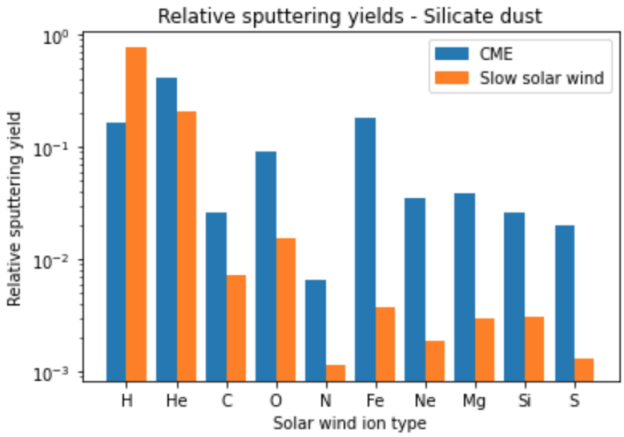

Figure 4.5: Relative sputtering yields in slow solar wind and CME conditions, for silicate dust.

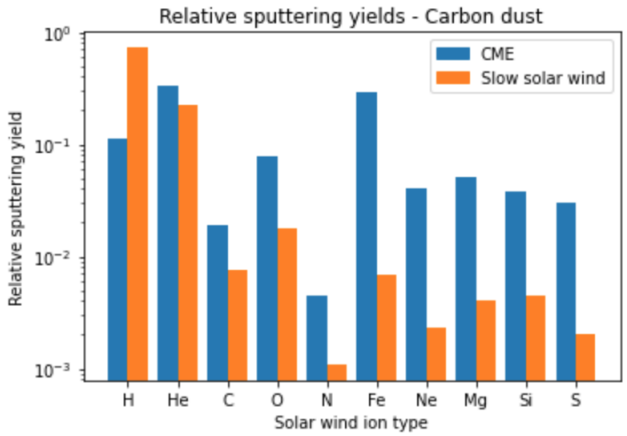

Figure 4.6: Relative sputtering yields in slow solar wind and CME conditions, for carbon dust.

Figures 4.4 - 4.6 show that hydrogen and helium account for the majority of the total sputtering combined during slow solar wind. This is the case for all three dust materials. Under CME conditions on the other hand, the heavier elements contribute significantly to the total sputtering yield as well. The reader is encouraged to note the logarithmic scale of the relative sputtering yields. For slow solar wind conditions, most of the heavy elements account for less than 1% of the total sputtering yield each. For CME conditions, the same value is between 1-10% for most heavier elements.

The figures also show that the relative sputtering yield of a given solar wind ion type varies with the dust material. While it may not be apparent from the figures above right away, an example that is more easily noticeable than others is the relative sputtering yield of iron. This value is higher for carbon dust than it is for metal oxide and silicate dust. Similar variations are found for the other solar wind ion types as well. This is an indicator of the material dependence of the sputtering yield. Another indicator of this dependency can be noticed by comparing the relative sputtering yield plots to Figure 3.2, the composition of the solar wind. Both are plots of fractions of whole quantity, total sputtering yield or the entire composition of the solar wind, and if the sputtering yield were not dependent on material or the sputtering efficiency of different ions, these should be equal. However, iron, for example, composes approximately 1% of the solar wind under CME conditions, but accounts for over 10% of the total sputtering yield.

The results of the sputtering yield calculations show that the solar wind condition a dust grain is exposed to, as well as the material it is composed of, is important when determining how much the sputtering can affect the dust.

The calculations of sputtering mass loss rate and lifetime is therefore done including both solar wind conditions and all three materials.

Sputtering mass loss rate

The sputtering mass loss rate is calculated from Equation 2.8, for the three dust sizes selected in Section 3.2.4: $r_d = 20$ nm, $r_d = 200$ nm and $r_d = 2$ μm. Figure 4.7 shows the result for slow solar wind conditions, while Figure 4.8 shows the result for CME conditions. In both figures, the sputtering mass loss rate is plotted as a function of distance from the Sun, for metal oxide, silicate and carbon dust.

For the discussion of the results, the dependencies of the sputtering mass loss rate is summarized here as a reminder for the reader. It is calculated from the solar wind flux f_{SW}, the total sputtering yield Y_{tot}, the cross section of the dust A and the mean atomic mass of the sputtered atoms m_A.

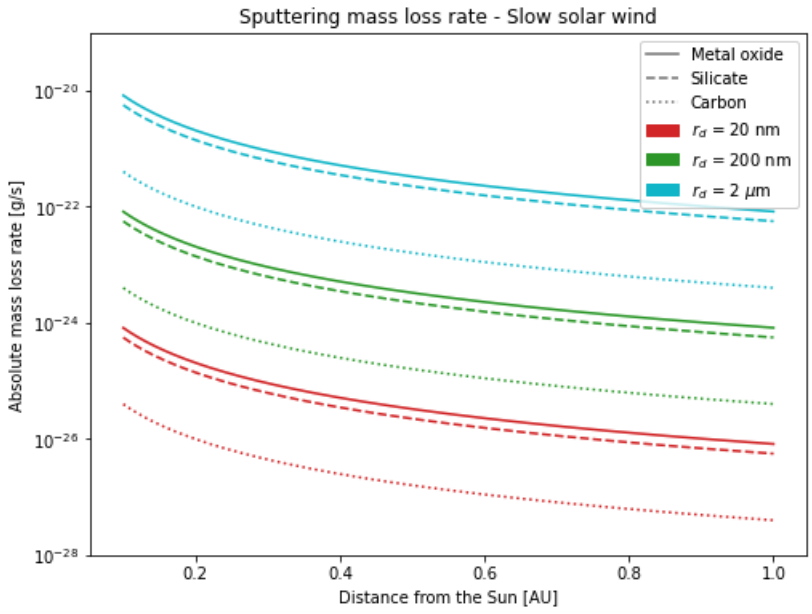

Figure 4.7: Sputtering mass loss rate under slow solar wind conditions, for three dust grains with radii of 20 nm, 200 nm and 2 μm of three different types of materials; metal oxide, silicate and carbon dust.

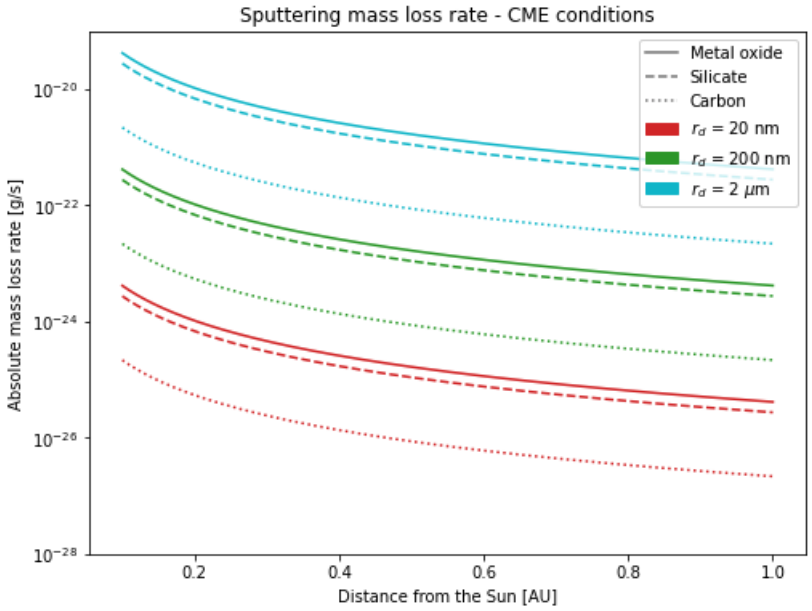

Figure 4.8: Sputtering mass loss rate under CME conditions, for three dust grains with radii of 20 nm, 200 nm and 2 μm of three different types of materials; metal oxide, silicate and carbon dust.

There are four main variables to notice when reading the figures; the size and composition of the dust, the solar wind condition and the distance from the Sun. Figures 4.7 and 4.8 show that the sputtering mass loss rate is higher for the larger grains. This can be understood from its dependence on A, the cross section of the grain, seen in Equation 2.8. Since the cross section increases with the dust radius, the grain is increasingly subjected to the solar wind flux with increasing dust size as well.

Further, the figures both show that the mass loss rate is highest for metal oxide dust and lowest for carbon dust. A contributing factor to this is the mean atomic mass m_A. The values for these constants are listed in Appendix A, and they show that the mean atomic mass is the highest for metal oxide dust, and the lowest for carbon dust. Another reason can be seen from the values for the sputtering yields, presented in Figure 4.3 and Table 4.1. For each solar wind condition, metal oxide dust has the highest sputtering yield, and carbon the lowest. An interesting point to notice is that the sputtering yield of silicate dust in CME conditions is higher than the sputtering yield of metal oxide dust in slow solar wind conditions. The effect of this on the mass loss rate illustrates the importance of the sputtering yield parameter, and can be seen from Figures 4.7 and 4.8, for example by considering the 2 μm dust grain at 0.2 AU from the

Sun. In this example, the mass loss rate is of an order of approximately 10^{-20} g/s for silicate dust in CME conditions and of an order closer to 10^{-21} g/s for metal oxide dust in slow solar wind conditions. The difference between the materials may therefore be explained by the different sputtering yields and mean atom mass values.

Another noticeable part of the results is the overall increase in mass loss rate when the dust is exposed to CME conditions. As mentioned already, the sputtering yield is significantly higher during a CME event, and so the dust is sputtered more efficiently and loses mass at a higher rate. Additionally, the solar wind speed increases during a CME event, which in turn also increases the solar wind flux f_{SW}. This relation is shown in Equation 3.6. In these calculations, the slow solar wind speed is estimated to be 300 km/s, while the CME wind speed is estimated to be 500 km/s, described in Chapter 3. It should be noted that the wind speed during a CME event can vary considerably, and may in some cases exceed 1000 km/s. Such circumstances would increase the mass loss rate even further. However, the average observed solar wind speed during CME events is between 400 km/s and 500 km/s (Ragot and Kahler, 2003), and so the estimate used here is considered adequate for the purpose of this project.

Finally, the results also show that the mass loss rate decreases with increasing distance from the Sun. This dependence is introduced by the solar wind flux, which decreases with distance as r^{-2}, due to the plasma density profile $n_p(r)$. The distance-dependence is presented in Equations 3.6 and 3.7. This means that dust close to the Sun loses mass at a higher rate than dust farther away, and sputtering may therefore play a more important role in the inner solar system than at larger distances.

Sputtering lifetime

The initial dust masses corresponding to the three dust radii of 20 nm, 200 nm and 2 μm are of orders 10^{-17} g, 10^{-14} g and 10^{-11} g, respectively. When they are exposed to the slow solar wind, the sputtering mass loss rates for the three grains are of orders of approximately 10^{-24} g/s, 10^{-22} g/s and 10^{-20} g/s at 0.1 AU from the Sun (from Figure 4.7, considering metal oxide dust as an example). While these numbers are 7-9 orders of magnitudes lower than the initial masses of the dust grains, the resulting mass loss may become of significance over time. A way to quantify this significance is to calculate the amount of time it takes before the dust is destroyed by the sputtering process. The sputtering lifetimes of the three dust grains are calculated using Equation 3.5, and the results are presented in Figure 4.9 for slow solar wind conditions, and in Figure 4.10 for CME conditions.

Thus far, in the discussion of the sputtering calculations, CMEs have been regarded in the same way as the slow solar wind conditions; as a general solar wind condition with a set of properties that affect the dust subjected to it. In view of sputtering lifetimes, it is important to consider the nature of CME events. As opposed to the slow solar wind, they are short-lived events with an average duration shorter than $1-2$ days (Baumann et al., 2020). Studies of CME events with very high wind speeds estimate the average duration of the events to be as short as 1 hour (Ragot and Kahler, 2003)). Nonetheless, the duration is significantly shorter than most dust lifetimes. The plotted lifetimes in Figure 4.10 show how long it takes for the dust to be destroyed by sputtering if it is subjected to CME conditions for the entirety of its lifetime. This is however not a realistic view for most dust grains. If the mass loss rate is adequately high and the dust grain is small enough, however, it might be the case that the dust is destroyed during a single CME event. For example, Baumann et al. (2020) show that this is the case for a 1 nm dust grain at a distance of 0.1 AU. For larger grains though, a more plausible picture is that the dust mainly experiences slow solar wind conditions, while occasionally being affected by occurring CME events. The results presented in Figure 4.10 should therefore be regarded accordingly.

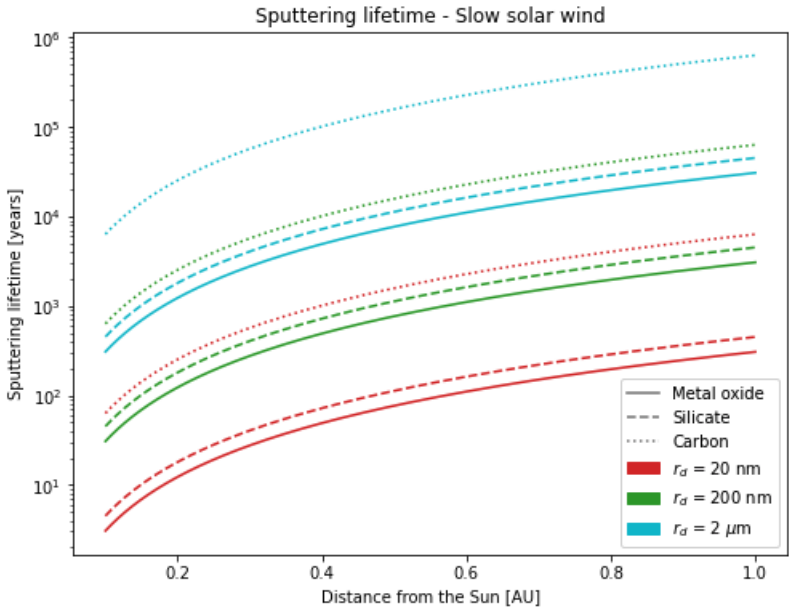

Figure 4.9: Sputtering lifetime in slow solar wind conditions, for three dust grains with radii of 20 nm, 200 nm and 2 μm of three different types of dust.

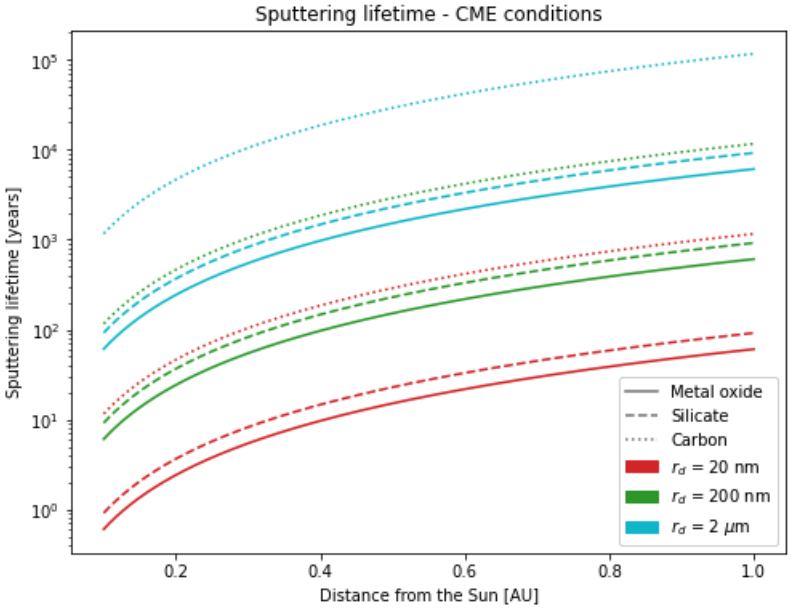

Figure 4.10: Sputtering lifetime in CME conditions, for three dust grains with radii of 20 nm, 200 nm and 2 μm of three different types of dust.

Figure 4.9 shows that under slow solar wind conditions the 20 nm grain of metal oxide dust has the shortest sputtering lifetime, ranging from around 3 years at 0.1 AU to around 312 years at 1 AU. The longest lifetime is found for 2 μm carbon dust, ranging from around 6441 years at 0.1 AU to 644100 years at 1 AU. The dust lifetime is inversely proportional to the mass loss rate, and so parameters that were discussed above regarding the mass loss rates contribute to this wide range of lifetimes as well. An interesting point to notice in the calculated lifetimes that was not already discussed in light of the mass loss rates, is that here, there is an overlap between values for different sizes. Since the mass loss rate for carbon dust is quite low compared to the other two materials, its resulting lifetime is higher as well. In calculating the lifetime, the mass of the dust is divided by the mass loss rate, and as seen in the figure, the lifetime of the 20 nm carbon dust exceeds the lifetime of the 200 nm metal oxide and silicate dust. Similarly, the 200 nm carbon dust exceeds the lifetime of the 2 μm metal oxide and silicate dust.

This section has presented the calculated sputtering yields for slow solar wind and CME conditions, for metal oxide, silicate and carbon dust. The mass loss rates at distances between 0.1 AU and 1 AU from the Sun for dust grains with radii 20 nm, 200 nm and 2 μm was presented, along with the corresponding sputtering lifetimes. The calculations show that the sputtering process may be of importance for dust grains close to the Sun, because of their small size. Additionally, the results show the that the sputtering mass loss rate varies with dust size and distance from the Sun, and so the significance of the process compared to collisions as destruction process vary with these parameters as well. The following section compares these two processes, and investigates this further.

4.2 Comparing mass loss processes outside of the sublimation zone

As discussed in Section 2.4.1, there is a dust free zone close to the Sun where the dust is destroyed by sublimation. The sublimation lifetimes calculated here, presented in Section 4.1.2, concur with commonly agreed upon estimates of a sublimation zone within 0.1 AU (Mann et al., 2004). Since the sublimation lifetime is very short at distances closer to the Sun than 0.1 AU, this thesis considers sublimation to be the dominating mass loss process in that region. Further, due to the steep increase in sublimation lifetime with increasing distance (see for example Baumann et al. (2020)), the mass loss due to sublimation is neglected outside of the sublimation zone in the following discussion.

The sputtering lifetimes calculated in Section 4.1.3 show that sputtering may be a significant mass loss process for dust outside of 0.1 AU. In this region however, the dust may also be destroyed by a collision with another dust grain. Both mass loss processes depend on the size of the dust as well as the distance from the Sun (Grün et al. (1985), Baumann et al. (2020)). This section compares the sputtering- and collision lifetimes to investigate which mass loss process is dominant for dust of different sizes and at different distances.

4.2.1 Lifetimes as function of distance - for selected sizes

The sputtering lifetimes under slow solar wind conditions, of metal oxide, silicate and carbon dust is plotted as functions of distance, together with the collision lifetime. Figures 4.11, 4.12 and 4.13 show the lifetimes for dust with a radii of 20 nm, 200 nm and 2 μm, respectively. The lifetimes are calculated and plotted for distances between 0.1 AU and 5 AU. The wide range in distance is chosen because of the previously discussed and derived distance-dependencies of both lifetimes. These do not vary as steeply as for example the sublimation lifetime, and so the lifetimes at large distances are included to illustrate the behavior of the functions with distance.

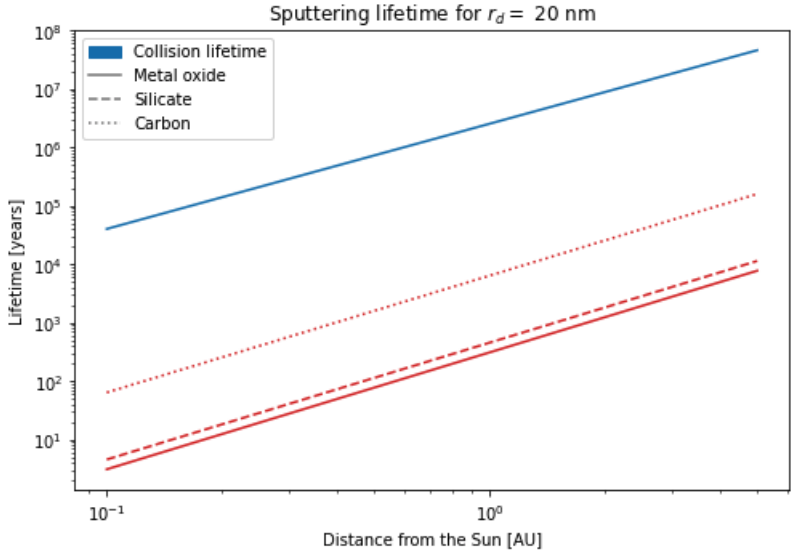

Figure 4.11: Sputtering lifetime in slow solar wind conditions, for the 20 nm dust grain and three different types of dust, plotted with the collision lifetime for this dust grain for comparison.

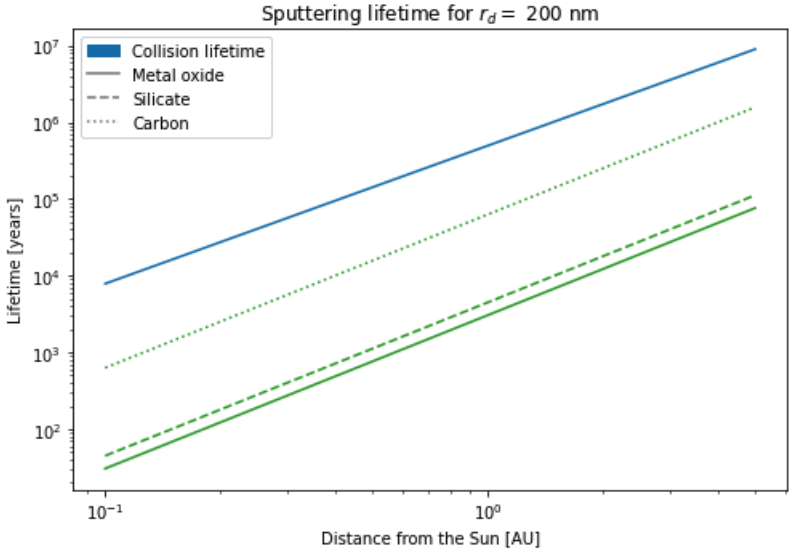

Figure 4.12: Sputtering lifetime in slow solar wind conditions, for the 200 nm dust grain and three different types of dust, plotted with the collision lifetime for this dust grain for comparison.

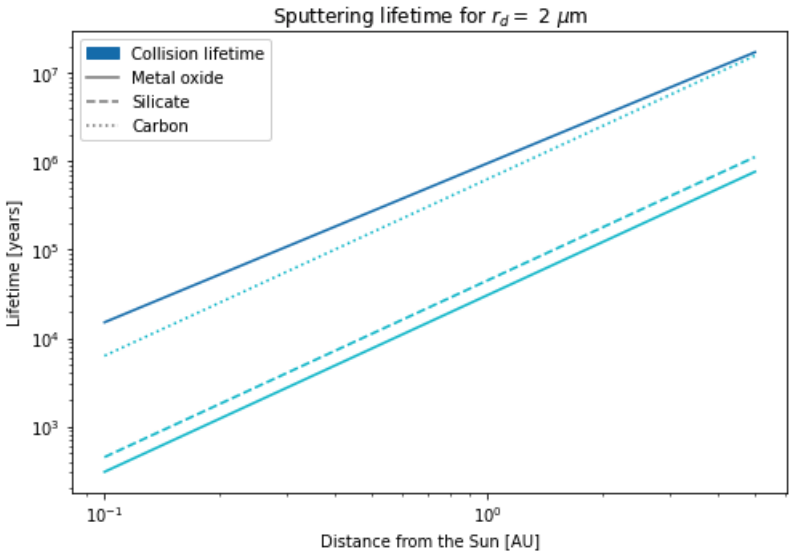

Figure 4.13: Sputtering lifetime in slow solar wind conditions, for the 2 μm dust grain and three different types of dust, plotted with the collision lifetime for this dust grain for comparison.

The lifetimes plotted in Figure 4.11 show that the sputtering lifetimes for the 20 nm dust grain is between approximately $3 - 4$ orders of magnitude lower than the collision lifetime, at distances between 0.1 AU to 5 AU. This means that sputtering is to be considered as the dominant mass loss function here, because the dust grain will be destroyed by the sputtering before it is likely to collide with another dust grain. Next, the lifetimes plotted in Figure 4.12 show that the sputtering lifetimes are shorter than the collision lifetimes for the 200 nm dust grain as well. The difference between the two processes is smaller for this size however, with the sputtering lifetimes being between approximately $1 - 3$ orders of magnitude lower than the collision lifetimes. A result that becomes more apparent in this plot is that the difference between the sputtering- and collision lifetime seems to decrease with distance, seen for the carbon dust. Finally, Figure 4.13 shows the lifetimes for the 2 μm dust grain. Here, the sputtering lifetimes are lower than the collision lifetime by approximately $0 - 2$ orders of magnitude. While the sputtering lifetime for carbon dust approaches the collision lifetime with distance for this size, the curves do not appear to cross each other within 5 AU. This means that for these three dust sizes, sputtering can be considered the dominating mass loss process between 0.1 AU and 5 AU.

An noticeable tendency in Figures 4.11 to 4.13 is that with increasing dust size, the distance at which the sputtering lifetime exceeds the collision lifetime, decreases. This distance is referred to as the critical distance henceforth. The

different slopes of the sputtering- and collision lifetimes is more apparent in the plot for the 2 μm grain, where the critical distance is almost reached within the plotted distance range for the carbon dust. This tendency suggests that there is a critical distance for all three dust grains outside of 5 AU, where sputtering can be neglected and collision considered the dominant mass loss process. However, for this thesis, the region of interest is the inner solar system. Therefore, it is more relevant to consider the tendency in the following manner. Since the increase in dust size suggests a decrease in critical distance, an interesting question is whether there is a certain range of sizes that result in a critical distance closer to the Sun. This is investigated further below.

4.2.2 Lifetimes as function of size - for selected distances

The sputtering- and collision lifetimes as a function of dust size is plotted for two selected distances, at 0.1 AU and 1 AU. These distances are chosen to limit the range of distances in which an occurrence of a critical distance is of interest in context of this thesis. For example, the critical distance of 2 μm carbon dust was found to be close to 5 AU from Figure 4.13, which is outside the region of interest here. Instead, the questions of whether there is a range of dust sizes that result in a critical distance between 0.1 AU and 1 AU is addressed. Figure 4.14, 4.15 and 4.15 show the results for metal oxide, silicate and carbon dust, respectively.

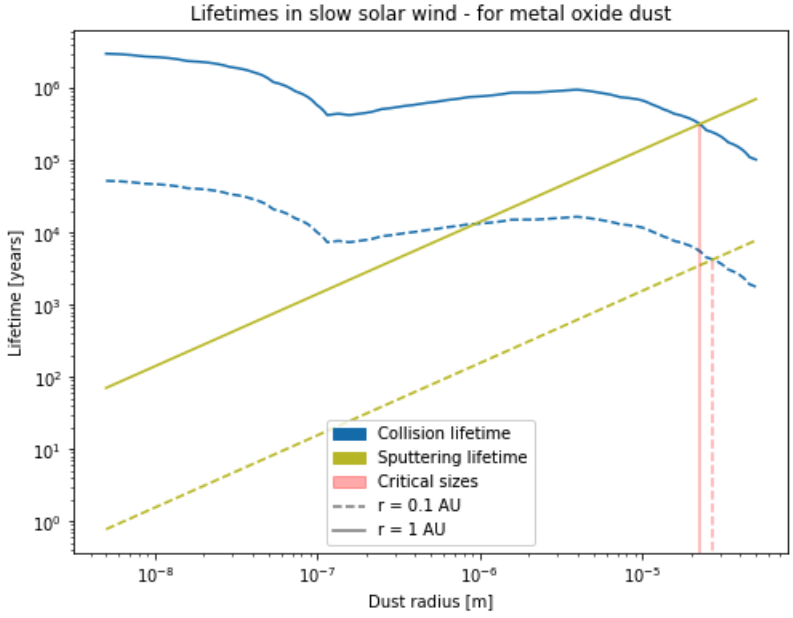

Figure 4.14: Sputtering lifetime and collision lifetime for metal oxide dust, as functions of dust radius, for two distances: $r = 0.1$ AU and $r = 1$ AU

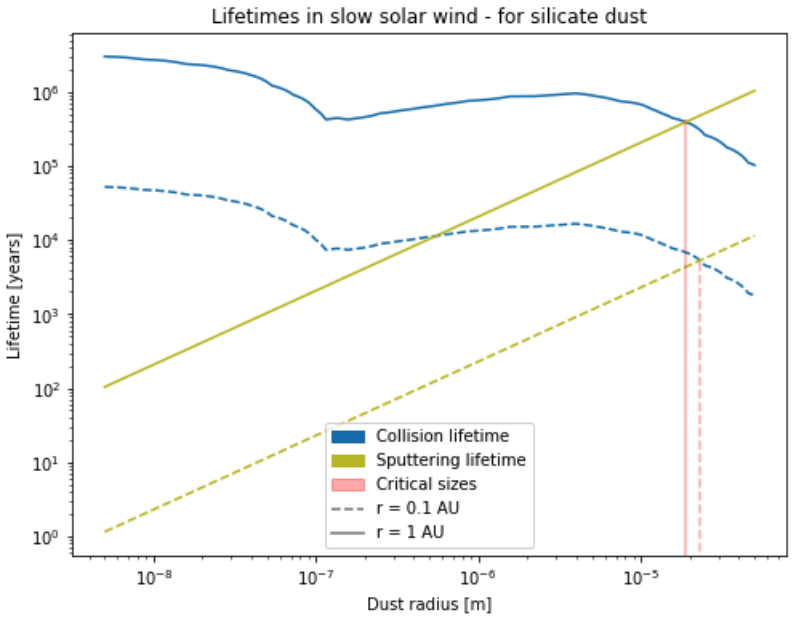

Figure 4.15: Sputtering lifetime and collision lifetime for silicate dust, as functions of dust radius, for two distances: $r = 0.1$ AU and $r = 1$ AU

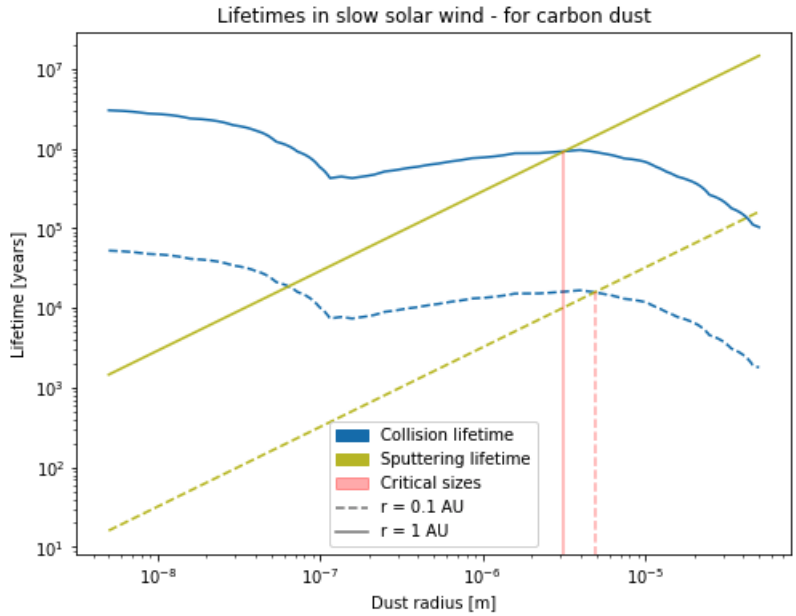

Figure 4.16: Sputtering lifetime and collision lifetime for carbon dust, as functions of dust radius, for two distances: $r = 0.1$ AU and $r = 1$ AU

In all three figures, the dashed and solid line plots show the lifetimes at 0.1 AU and 1 AU, respectively. The red, vertical lines are included to highlight the dust radius where the sputtering lifetime exceeds the collision lifetime. This is referred to as the critical size of the dust henceforth. For all three materials, the critical size is smaller at 1 AU than at 0.1 AU. In light of the results presented in Figures 4.11-4.13, where increasing the dust size decreased the critical distance, this result is expected. For example, if a fourth dust size, larger than the 2 μm dust grain, had been considered, this would have decreased the critical distance closer to 1 AU. If then an even larger grain had been considered, the critical distance would have decreased to approach 0.1 AU. Another part of these results that should be mentioned is that the critical sizes of carbon dust are lower than the critical sizes for the other two dust materials. As shown in Section 4.1.3 from the sputtering calculations, the sputtering lifetime is considerably higher for carbon dust than for metal oxide and silicate dust. Here, that means that the curve for carbon dust crosses the curve for the collision lifetime at a lower dust radius, resulting in a lower critical size.

The approach of plotting both of the lifetimes as function of mass allows for a way of determining the critical sizes numerically. The code written to calculate and plot the results iterates through the curves at equal distances and finds the point where they intersect. The corresponding dust radius is the critical size. This is done for Figures 4.14 - 4.16, and the results are included in Table 4.2. The above results are for slow solar wind conditions, and for comparison, the same calculations are performed for CME conditions. The resulting critical sizes are included in Table 4.2 as well.

	SSW		CME	
	r = 0.1 AU	r = 1 AU	r = 0.1 AU	r = 1 AU
Metal oxide dust	27 μm	22 μm	$>$ 50 μm	44 μm
Silicate dust	23 μm	19 μm	44 μm	38 μm
Carbon dust	5 μm	3 μm	14 μm	11 μm

Table 4.2: Critical dust radius, i.e. where collision lifetime is lower than sputtering lifetime, for distances, $r = 0.1$ AU and $r = 1$ AU, for three dust materials. Numbers for both slow solar wind (SSW) and CME conditions are included.

When performing these calculations, nested matrices of sputtering- and collision lifetimes for sizes between 5 nm and 50 μm and distances between 0.1 AU and 5 AU were generated in the code. The critical size at these distances was determined in the same manner as described above, and the result is included in Figure B.1 in Appendix B.

4.2.3 Evaluating the dominant mass loss processes

From the results presented in this section thus far, sublimation is considered the dominant mass loss process inside of 0.1 AU. Outside of this sublimation zone however, the dominant mass loss process depends on the size of the dust. At 0.1 AU during slow solar wind conditions, sputtering is found to be the dominating mass loss process for dust with radii smaller than 27 μm, 23 μm and 5 μm, for metal oxide, silicate and carbon dust, respectively. The same values are 22 μm, 19 μm and 3 μm at 1 AU. This means that for nanometer-sized dust and for grains of a few micrometers, sputtering is the dominant mass loss process between 0.1 AU and 1 AU. At larger sizes, the dust grains are likely to be destroyed by a collision before it is destroyed by sputtering. Collisions are thus considered the dominating mass loss process for these grains.

This primary objective of this thesis is to investigate the effect of mass loss on the dust trajectories. Whether the dominant mass loss process is sputtering or collisions is therefore of importance in the context of the thesis for the following reason. If the dust is destroyed by a collision, the mass can be considered constant until it is destroyed by a single event. While the grain arguably loses its mass, this would not be seen in the dust trajectory, as it is a short-lived process. However, the sputtering process is an erosive process, and so a gradual change in mass along the trajectory could affect the orbit over time. The values calculated in this section provide a size limit to the dust where the influence of sputtering on the dust dynamics should be evaluated. The dust grains that have been considered thus far, with radii of 20 nm, 200 nm and 2 μm are all within the the size range where sputtering is the dominating mass loss process between 0.1 AU and 1 AU. Thus, these are considered in the orbit calculations following this section as well.

4.3 Verification of the implemented numerical method

The code written to perform the orbital calculations as described in Chapter 3 is here verified by considering a set of dust grains with constant β-values. The calculated trajectories of these grains are compared to the expected behavior of β-meteoroids initially in circular orbits, as discussed in Chapter 2. An error estimate is given for both the Euler-Cromer method and the Leapfrog integration method by comparing the numerically calculated orbits to a known analytical solution. The source region of the dust is a user defined parameter in the code, and so for the case of $\beta = 0$, hence a circular orbit, the distance between the dust and the Sun is constant and a known parameter. Figure 4.17 shows the calculated trajectories of six dust grains with different constant β-values. The calculated error estimates of both numerical methods are presented in Figure 4.18.

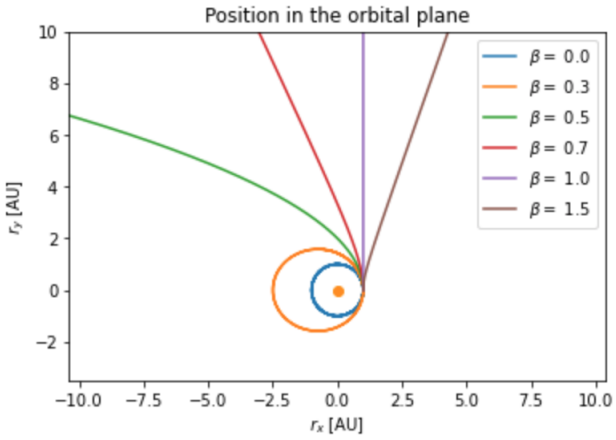

Figure 4.17: Trajectories of dust grains with constant mass, calculated and plotted for different β-values. The orange marker at (0, 0) AU is included to illustrate the position of the Sun. The figure is adapted from a project completed by the author in preparation for this thesis work.

When dust grains initially are in bound, circular orbits, and then are subjected to the solar radiation pressure force, the expected behavior is that dust with $\beta = 0$ remain in circular orbits. Figure 4.17 shows that the calculated orbit is as expected for this case, seen in the blue line plot. Elliptical orbits are expected for dust with $0 < \beta < 0.5$, which is confirmed for the case where $\beta = 0.3$, seen in the orange line plot in the figure. Next, when $\beta = 0.5$, the dust is ejected from the solar system in a parabolic orbit, as seen in the green line plot in the figure. The calculated trajectories for $\beta = 0.7, 1.0$ and 1.5 show that the dust is ejected in hyperbolic orbits, also as expected.

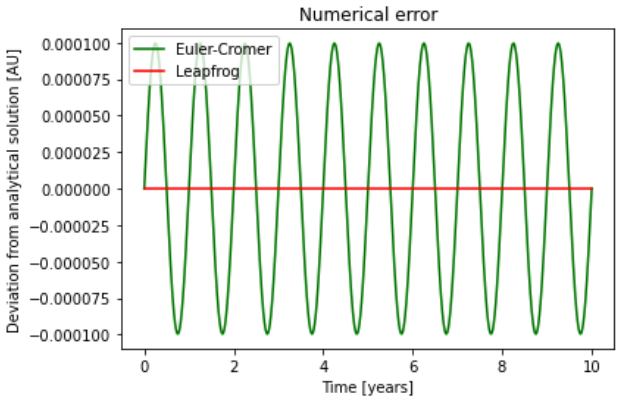

Figure 4.18: Numerical error estimates for the Euler-Cromer and Leapfrog integration method, estimated by comparing the length of the position vector r of the numerical solutions to the analytical solution for a circular orbit with known radius. The errors are calculated for a time step of $dt = 1000$s.

The error estimates for the Euler-Cromer method and the Leapfrog integration method are presented in Figure 4.18, derived by comparing the numerically calculated position vector r to the analytically known solution. Specifically, a circular orbit with radius of 1 AU is considered, and the deviation from this length for each numerical solution is included in the plot. The errors for the Euler-Cromer method are of orders of $10^{-5} - 10^{-4}$ AU, and are visibly greater than the errors of the Leapfrog integrator. While not apparent from the figure, the Leapfrog errors are of orders 10^{-8} AU, and due to its higher accuracy, it is the chosen method for the orbit calculations performed in this thesis work. A plot of the Leapfrog integration method is included in Figure 4.19 for illustration.

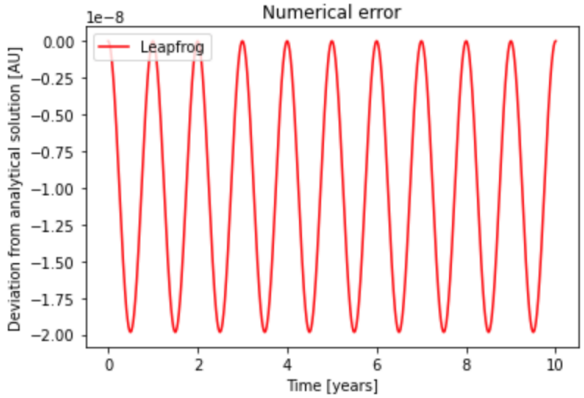

Figure 4.19: Numerical error estimates for the Leapfrog integration method. The errors are calculated for a time step of $dt = 1000$s.

4.4 Orbital calculations for low β-value fragments

Throughout this thesis, three dust grains with radii of 20 nm, 200 nm and 2 μm have been considered. The 200 nm dust grain is a β-meteoroid with a high initial β-value of 0.85, calculated from the values provided by Wilck and Mann (1996). The orbital calculations for this grain are included in Section 4.5. The 20 nm and 2 μm grains on the other hand, have low initial β-values of 0.047 and 0.097, respectively, meaning that they are in bound orbits with low eccentricities. This section presents and discusses the orbital calculations performed for these two grains. For both grains, the source region of the dust is considered to be at 0.2 AU from the Sun. Mass loss due to sputtering is applied along the trajectories, as this was determined the dominant mass loss process at this distance and for the considered dust sizes. Slow solar wind conditions are considered in the calculations. The grains may occasionally experience CME events along their trajectories, which could be of significance for the 20 nm grain in particular, because of its low mass. Due to the short-lived nature of the CME events however, slow solar wind is considered throughout the entire orbit as a first approach. While the sputtering mass loss rate varies with the material of the dust, as seen for example in Figure 4.7, the resulting variation in the orbital calculations is not visible in the trajectory plots. Therefore, only the results for silicate dust grains are included here.

Results for the 20 nm dust grain

Figure 4.20 shows the calculated trajectory of the 20 nm dust grain. The initial position of the dust is at $(0.2, 0)$ AU. The dust completes several revolutions around the Sun before it is destroyed after around 20 years, and each of these orbits are plotted on top of each other in the figure to illustrate the general behavior of the dust motion. To better show the evolution of the orbits as the dust is subjected to a mass loss, the perihelion- and aphelion distances throughout the dust lifetime are presented in Figure 4.21 and 4.22, respectively.

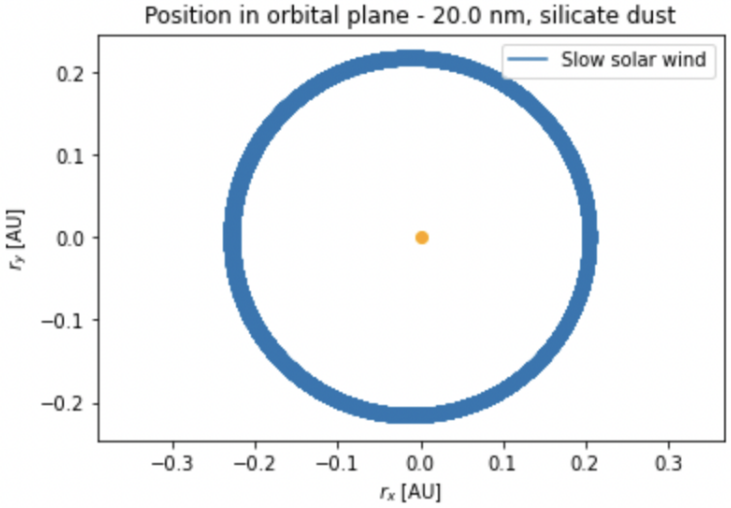

Figure 4.20: Position in the orbital plane for a 20 nm silicate dust grain initially at a distance of 0.2 AU from the Sun. The dust is subjected to sputtering, and all completed orbits are included and plotted on top of each other. The orange marker at (0,0) AU is included to show the position of the Sun.

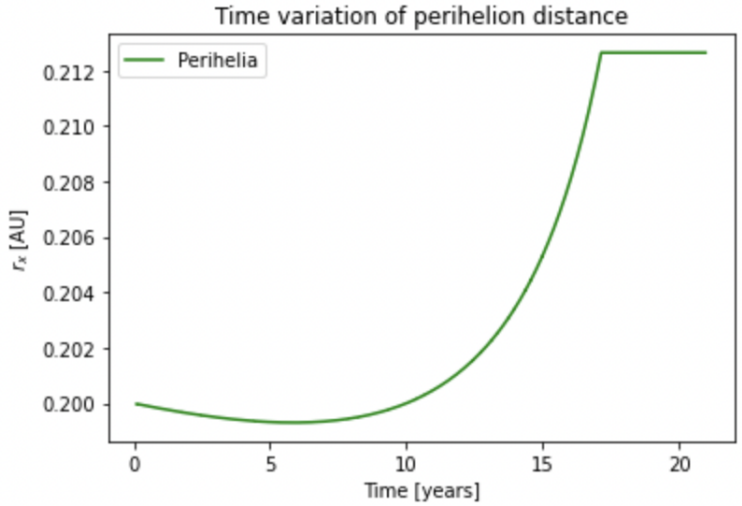

Figure 4.21: Time variation of the perihelion distance, for a 20 nm silicate dust grain subjected to sputtering along its trajectory. The initial distance of the dust is 0.2 AU from the Sun.

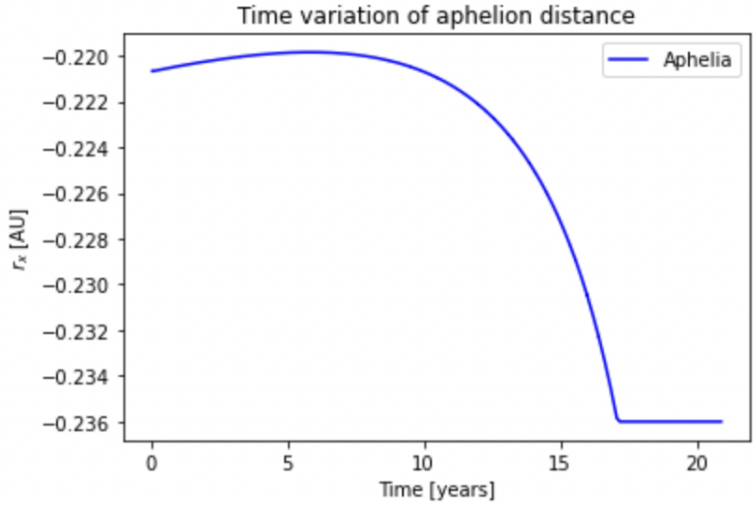

Figure 4.22: Time variation of the aphelion distance, for a 20 nm silicate dust grain subjected to sputtering along its trajectory. The initial perihelion of the dust is 0.2 AU from the Sun.

With an initial β-value of 0.047, the orbit of the 20 nm dust grain is close to circular, as can be seen in Figure 4.20. Due to the mass loss along its trajectory, the β-value varies during the orbits, resulting in the drift of the dust apparent in the figure. Figure 3.3 showing the relation of β as function of mass shows that the 20 nm dust grain with mass of order 10^{-17} g first experiences a small decrease in β and then an increase up to the lower limit of the interpolation range at $\beta = 0.106$. During the decrease, the orbit becomes more circular, resulting in an inwards drift of the dust. Then, during the increase, the orbit becomes more elliptical, that is, the eccentricity increases, and the dust drifts outwards. Since the orbits are plotted on top of each other, this variation in time is not apparent from the plot of the position in the orbital plane. The drift is therefore better seen in Figures 4.21 and 4.22. Here, it can be seen that both the perihelia and aphelia move closer to the Sun during approximately the first 6 years, before they move further away from the Sun again. This turning point in time is when the β-value starts to increase. At around 17 years, the lower limit of the interpolation range of the data is reached, and the constant values of the perihelion and aphelion distances are artifacts of the implemented program. In the function where $\beta(m)$ is calculated in the code, the β-value is set equal to the lowest known value from Wilck and Mann (1996) if the mass reaches the lower limit in their data. Since the 20 nm grain is eventually destroyed, this is what occurs here and what causes the constant values observed in the figures.

While the orbits are close to circular, there is a small eccentricity and therefore a difference between the perihelion and aphelion distance of the orbit. This means that the sputtering mass loss rate is higher at the perihelion, causing the dust to lose more mass in this region. Because of the larger distance from the Sun, the dust loses less mass around the aphelion. The result of this can be seen in the overall change in perihelia compared to the change in aphelia. From Figures 4.21 and 4.22, the total time variation of the aphelion distances is larger than that of the perihelion distances. Both of these drifts are of orders 10^{-2} AU. The numerical errors of the calculations are of order 10^{-8} AU, and are therefore not considered significant to these results.

The dust radius of 20 nm was selected in this thesis as an example of the population of dust with masses in the range on the left hand side of the green, filled area in Figure 3.3. This dust grain therefore represents dust that is smaller than β-meteoroids. In general, these results verify that these dust grains may be destroyed by sputtering in the inner solar system, as expected from the sputtering lifetimes presented in Figure 4.9. The calculations also illustrate that the sputtering process can result in an outward or inward drift for particles of this size. An important note regarding the dust motion observed in these calculations is that the only forces included in the equation of motion here are the gravitational pull the Sun and the solar radiation pressure force. As previously mentioned, the motion of dust smaller than around 100 nm may also be affected by the Lorentz force (Mann and Czechowski, 2021). The trajectory of the 20 nm grain shown here may therefore not represent a realistic dust motion for grains of this size, as the Lorentz force could affect the trajectory as well. For the purpose of examining the effect of mass loss on the dust trajectory however, the results show that the sputtering process can play a role in the dust motion as well. The plots in Figures 4.20 - 4.22 should therefore be regarded in view of this, and seen as an illustration of the effect of the sputtering process alone.

Results for the 2 μm dust grain

The calculated trajectory of the 2 μm dust grain is presented in Figure 4.23. The initial position of the dust is $(0.2, 0)$ AU for this grain as well. The figure shows around 7000 completed orbits over around 600 years, and these are plotted on top of each other. The β-value of this dust grain is initially 0.097, and given its mass of order 10^{-11} g, β increases as a result of the mass loss. This can be seen from Figure 3.3. A drift is apparent also for this dust grain, and the time variations of the perihelion- and aphelion distances are plotted in Figure 4.24 and 4.25.

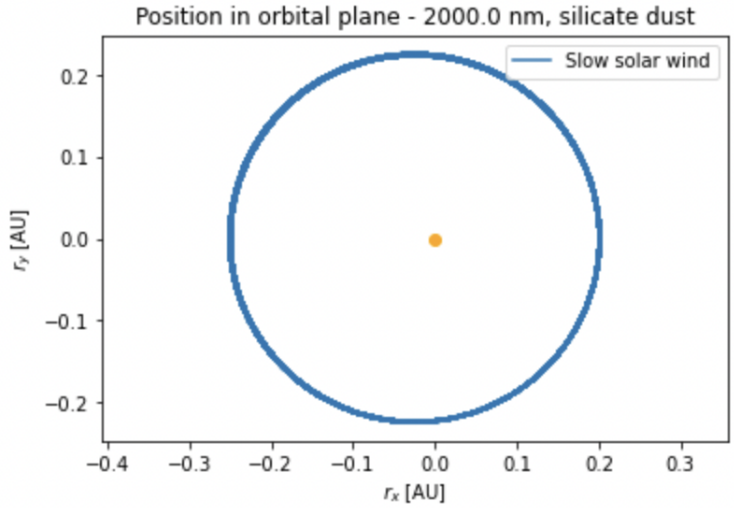

Figure 4.23: Position in the orbital plane of a 2 μm silicate dust grain initially at a distance of 0.2 AU from the Sun. The dust is subjected to sputtering along its trajectory, and the resulting orbits are plotted on top of each other. The orange marker at (0,0) AU is included to show the position of the Sun.

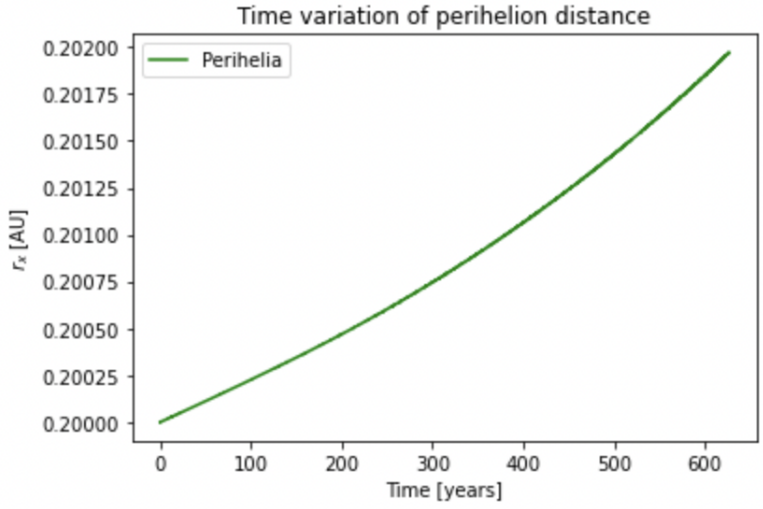

Figure 4.24: Time variation of perihelion distance, for a 2 μm silicate dust grain subjected to sputtering along its trajectory. It is initially at a distance of 0.2 AU from the Sun.

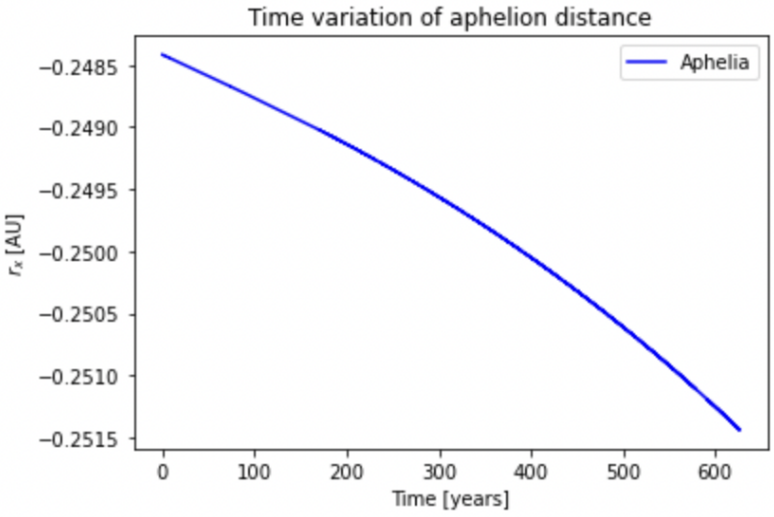

Figure 4.25: Time variation of aphelion distance, for a 2 μm silicate dust grain subjected to sputtering along its trajectory. The initial perihelion distance is 0.2 AU from the Sun.

The orbits for the 2 μm dust grain are also close to circular, because of the low initial β-value. This is shown in Figure 4.23. The initial mass of the dust is of order 10^{-11}, and so when the dust is subjected to sputtering along its trajectory, the β-value consequently increases. During the time span of the calculations presented above, approximately 600 years, the β-value increased from 0.097 to 0.107. This change results in an increasing eccentricity of the orbits and an outward drift of the dust, and Figures 4.24 and 4.25 show that both the perihelion- and aphelion distances move farther away from the Sun with time. The small eccentricity of the dust orbit results in a slight difference between the perihelion and aphelion also here, and so the dust is subjected to a higher mass loss rate in the perihelion than in the aphelion. The aphelion drift is therefore greater than than the perihelion drift, and this in turn causes the increase of the eccentricity of the orbit. As the orbit is close to circular, the changes are still both of orders 10^{-3} AU. The numerical error of order 10^{-8} AU is therefore not considerable for the purpose of this discussion.

The dust grain with a radius of 2 μm was selected as an example of the population of dust with masses in the range on the right hand side of the green, filled area in Figure 3.3. In other words, it represents dust that is larger than β-meteoroids. Dust of this size has a negligible charge-to-mass ratio, and the dust motion is not significantly affected by the Lorentz force (Mann and Czechowski, 2021). The dust motion calculated for this grain is therefore a more realistic result, compared to the results presented for the 20 nm dust grain.

However, an effect that becomes important for objects with high velocities near the Sun, such as dust particles, is the Poynting-Robertson effect. This effect is often referred to as a drag, because it contributes a tangential component to the radiation pressure force, towards the Sun. This means that dust grains orbiting the Sun experience an inward drift caused by this effect, and they are eventually dragged into the Sun (Grün et al., 1985). The amount of time this takes depends on the size of the dust, and its distance from the Sun, and is referred to as the Poynting-Robertson lifetime. Grün et al. (1985) provide estimates for this lifetime, for a range of masses between 10^{-18} g and 10^{2} g, at distances 0.1 AU and 1 AU from the Sun. The effect of sputtering on the dust motion is discussed in view of the Poynting-Robertson lifetime in the following section.

4.4.1 Sputtering as a production process of β-meteoroids

An open question regarding the influence of sputtering on the dynamics of dust near the Sun is whether it is a process that can produce β-meteoroids. As seen from the results of the orbital calculations performed for the 2 μm dust grain, sputtering increases the β-value and causes an outward drift of the dust. In theory, if this grain continues to lose mass and eventually obtains a β-value of 0.5, it is ejected from the Sun and becomes a β-meteoroid. A way to investigate the possibility that sputtering can produce β-meteoroids in this manner, is to calculate the amount of time necessary to reach $\beta = 0.5$ as a result of sputtering mass loss. Here, this is done by running the program calculating the orbits resulting from the mass loss, until $\beta = 0.5$. The resulting time is referred to as the sputtering ejection time henceforth. Without the presence of other effects, the ejection time would provide a timescale for sputtering production of β-meteoroids. However, while it has been shown in Figures 4.24 and 4.25 that the sputtering process increases the eccentricity of the dust orbit, the Poynting-Robertson effect simultaneously decreases it. As a first approach to evaluate whether the sputtering mass loss or the Poynting-Robertson effect governs the dust motion, the sputtering ejection time is compared to the Poynting-Robertson lifetime. Table 4.3 presents the numerically derived sputtering ejection times τ_e and includes estimates of the Poynting-Robertson lifetimes τ_{PR} from Grün et al. (1985).

	$r_0 = 0.1$ AU	$r_0 = 0.2$ AU	$r_0 = 0.3$ AU
τ_e [years]	657	2690	5917
τ_{PR} [years]	≈ 15	≈ 300	≈ 500

Table 4.3: Sputtering ejection times τ_e from numerical orbit calculations with an initial dust radius of 2 μm, and approximate Poynting-Robertson lifetimes τ_{PR} for 2 μm dust from Grün et al. (1985). The values are included for three source regions r_0 of the dust, 0.1 AU, 0.2 AU and 0.3 AU from the Sun.

The general results from the calculations are that the sputtering ejection lifetimes are shorter than the Poynting-Robertson lifetimes by approximately one order of magnitude. The nature of the two time estimates are not quite similar however, and so this direct comparison may not be entirely justifiable at first glance. Table 4.3 shows that the sputtering ejection time for a dust grain with an initial radius of 2 μm is 657 years with a source region at 0.1 AU, 2690 years with a source region at 0.2 AU and 5017 years with a source region of 0.3 AU from the Sun. These estimates take into account the size- and distance dependency of the sputtering mass loss rate, as they are numerically derived using the iterative method described in Chapter 3. The Poynting-Robertson estimates on the other hand, are the initial lifetimes of the dust and do account for the mass loss along the trajectory. The initial mass of the grain is of order 10^{-11} g, and from Figure 3.3, the final mass of the grain, in other words when $\beta = 0.5$ is reached, is between 10^{-11} g and 10^{-12} g. For dust within this size interval, the Poynting-Robertson lifetime decreases with mass loss Grün et al. (1985). This means that if the mass loss was accounted for, the Poynting-Robertson lifetimes that the sputtering ejection times are compared to would be even shorter. The estimates given in Table 4.3 can therefore be seen as an upper limit in terms of the mass dependency for this case. The Poynting-Robertson lifetime decreases with distance as well Grün et al. (1985), and since the effect itself results in an inward drift of the dust, the estimates are upper limits to the lifetimes in terms of the distance dependency as well. However, the sputtering contributes an outward drift of the dust, and so the ratio of the inward drift due to the Poynting-Robertson effect and the outward drift due to the sputtering mass loss is of interest. As a first approach, the drift rates at 0.2 AU are considered. The estimates in Table 4.3 show an inward drift rate of 0.2 AU per 300 years, which is a lower limit estimate of the drift rate, because 300 years is an upper limit as discussed above. Figures 4.24 and 4.25 show that the outward drift rate is of order 10^{-3} AU over 600 years. This suggests that the inward drift is in fact the dominant behavior of the dust orbit, even though there is an outward drift caused by the sputtering.

From the above discussion and the calculated sputtering ejection times for a 2 μm dust grain, it is concluded that sputtering is an unlikely production process of β-meteoroids, because the dust drifts inward by the Poynting-Robertson effect and reaches the Sun before it becomes a β-meteoroid. There may be dust grains with β-values very close to 0.5 initially, where the mass is reduced sufficiently by sputtering before it is dragged inwards by the Poynting-Robertson effect. However, because of the slope of $\beta(m)$, such cases do not cover a wide range of masses. They are therefore not considered further in this thesis, but make up an interesting possibility of a special case.

4.5 Orbital calculations for high β-value fragments

The dust grain with a radius of 200 nm that has been considered throughout the thesis was selected as an example of a β-meteoroid. The initial β-value of this dust grain is 0.85, and the initial mass is of order 10^{-14} g. This section presents and discusses the orbital calculations for this β-meteoroid.

Results for the 200 nm dust grain

The same conditions are considered here as for the 20 nm and 2 μm dust grains discussed in Section 4.4. Silicate dust initially at a distance of 0.2 AU from the Sun is subjected to slow solar wind, and experiences a mass loss due to sputtering along its trajectory. The resulting dust motion is calculated, and is presented in Figure 4.26.

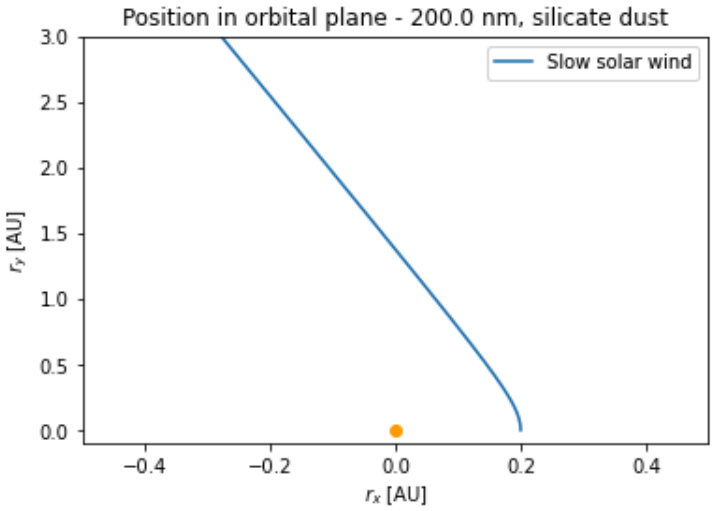

Figure 4.26: Position in the orbital plane of a 200 nm silicate dust grain initially at a distance of 0.2 AU from the Sun. The dust is subjected to sputtering along the trajectory. The orange marker at (0,0) AU is included to show the position of the Sun.

The figure shows that the dust is ejected from the solar system in a hyperbolic orbit, which is the expected motion of a β-meteoroid. From the orbital calculations of the low β-value fragments, where the dust grains were in bound orbits, the effect of the sputtering mass loss was observed as a drift of the orbits. A potential influence of the sputtering cannot be recognized in the same manner here, due to the unbound nature of the β-meteoroid orbit. Instead, evaluating the rate of change in the β-value resulting for the sputtering mass loss can be

a useful approach to investigate the influence of sputtering on β-meteoroids. This relates to another open question regarding sputtering, which is whether the process that can destroy or significantly reduce the size of β-meteoroids. The influence of sputtering on the 200 nm dust grain is discussed in light of this question in the following section.

4.5.1 Sputtering as a destruction process of β-meteoroids

Since the β-meteoroids are ejected from the solar system by the solar radiation pressure force, the distance to the Sun increases rapidly. The sputtering mass loss rate varies as function of distance with the solar wind flux as r^{-2}, and is therefore considerably reduced as the dust travels out of the inner solar system. This section investigates how the motion of β-meteoroids are influenced by the sputtering, by calculating the accumulated mass loss along the trajectory, until the mass loss is negligible. Based on these results, the possibility of sputtering being a destruction process of β-meteoroids is discussed.

To perform these calculations, a definition of a negligible value of mass loss is necessary. Since the orbits are calculated using the written program, and a mass loss value of zero is numerically unobtainable, several low values were considered as a condition for a negligible mass loss. In the results presented in Table 4.4, one atomic mass unit is used, so when the sputtering mass loss rate is below $1.66 \cdot 10^{-24}$ g/s, the program ends the calculations. Conditions of several orders lower than this value was investigated as well, however the difference in the results was not of high significance for the purpose of this discussion. Thus, the familiar physical constant of one atom mass unit is used instead of an arbitrary lower value. The final mass of the dust grain is compared to the initial dust mass of the 200 nm dust grain, and the resulting change in β-value is calculated as well. These calculations are performed for different source regions of the dust. The results are presented in Table 4.4.

Source region r_0	m_{end}/m_0	Δm	$\Delta\beta$
0.1 AU	0.99983	$1.42 \cdot 10^{-17}$ g	$2.89 \cdot 10^{-7}$
0.2 AU	0.99990	$8.74 \cdot 10^{-18}$ g	$1.77 \cdot 10^{-7}$
0.3 AU	0.99992	$6.02 \cdot 10^{-18}$ g	$1.22 \cdot 10^{-7}$
0.4 AU	0.99995	$4.14 \cdot 10^{-18}$ g	$8.39 \cdot 10^{-8}$
0.5 AU	0.99997	$2.51 \cdot 10^{-18}$ g	$5.06 \cdot 10^{-8}$

Table 4.4: Total mass loss and resulting change in β-value for a 200 nm dust grain subjected to sputtering on its trajectory out of the solar system. The final mass m_{end} is determined when the sputtering mass loss rate is smaller than one atomic mass unit per second.

The results presented in Table 4.4 show that sputtering influences β-meteoroids with source regions closer to the Sun the most, as expected. The total mass loss is of order 10^{-4} lower than initial mass at most, which results in a total change of β-value of order 10^{-7}. These results suggest that the sputtering does not significantly affect the motion of β-meteoroids. Further, the mass loss due to sputtering is low enough that the assumption that β-meteoroids have a constant mass is considered valid. This assumption is for example used by Szalay et al. (2020) in the derivation of the density model for β-meteoroids, as discussed in context of Equation 2.5. By the same reasoning, the sputtering process is not considered a process for destruction of β-meteoroids.

4.5.2 Influence of sputtering on fragments in highly elliptical orbits

The three dust sizes with radii 20 nm, 200 nm and 2 μm that have been considered throughout this work have initial β-values that are either so high that the dust is ejected, or so low that their orbits are close to circular. For the dust in bound orbits, a drift of the perihelion- and aphelion distances is observed as a result of the mass loss, which suggests that sputtering can be a process that contributes to the creation of dust rings in the solar system. The width of these dust rings depends on the magnitude of the drift, or in other words, how much the perihelion- and aphelion distances change. Due to the small eccentricity of the orbits, there is a small difference between the drift of the perihelia and the drift of the aphelia. This is because the dust loses mass at a higher rate closer to the Sun, and the change in the dust motion is consequently higher some places in the orbit than others. This difference is therefore expected to increase with eccentricity, and to further investigate this effect, a dust grain in a highly elliptical orbit is considered. In order to determine a dust size suitable for this, the mass corresponding to a β-value of 0.49 is found. There are two places on the $\beta(m)$ curve in Figure 3.3 where this is the case, one on the left hand side of the green, filled area, and one on the right hand side. When the sputtering mass loss rate is applied, the latter dust grain would be ejected, and the orbital drift would not be possible to evaluate. Therefore, a dust grain with $\beta = 0.49$ on the left hand side is chosen, as its β-value decreases with mass loss. The dust radius corresponding to this is 65 nm.

The orbital calculations for the dust grain with a radius of 65 nm is performed in the same manner as for the other considered dust grains. It is silicate dust, subjected to slow solar wind conditions. This dust size is also within the size range where sputtering was determined as the dominant mass loss process outside of 0.1 AU, as can be seen from Table 4.2. A mass loss due to sputtering is therefore applied along the dust trajectory, for a calculations are performed for 600 years. The resulting orbits are shown in Figure 4.27, and the perihelion- and aphelion distances are plotted in Figures 4.28 and 4.29. These are plotted together in Figure 4.30 for comparison.

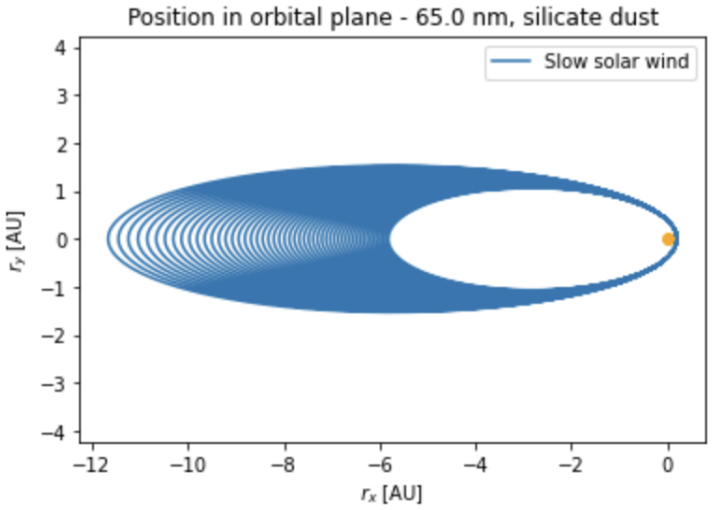

Figure 4.27: Position in the orbital plane of a 65 nm silicate dust grain initially at a distance of 0.2 AU from the Sun. The dust has an initial β-value of 0.49, and subjected to sputtering along its trajectory. The outermost orbit is the initial orbit, and the dust experiences an inward drift over time. The orange marker at (0,0) AU is included to show the position of the Sun.

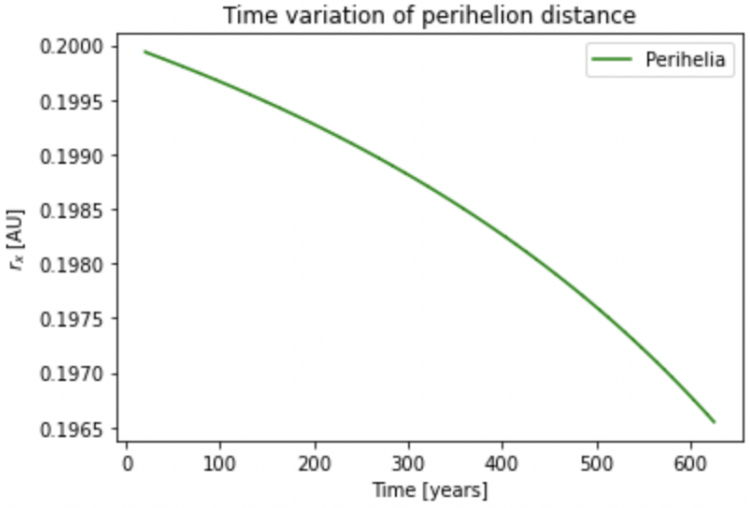

Figure 4.28: Time variation of perihelion distance, for a 65 nm silicate dust grain initially at a distance of 0.2 AU from the Sun.

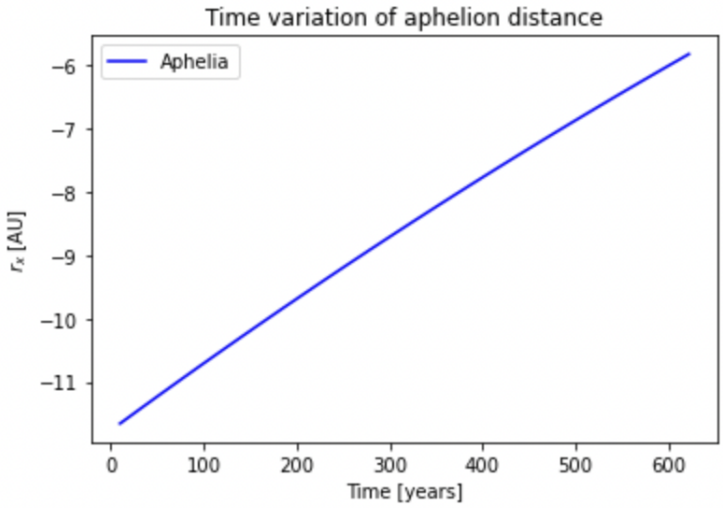

Figure 4.29: Time variation of aphelion distance, for a 65 nm silicate dust grain initially at a distance of 0.2 AU from the Sun. The dust has an initial β-value of 0.49, and is subjected to sputtering along its trajectory.

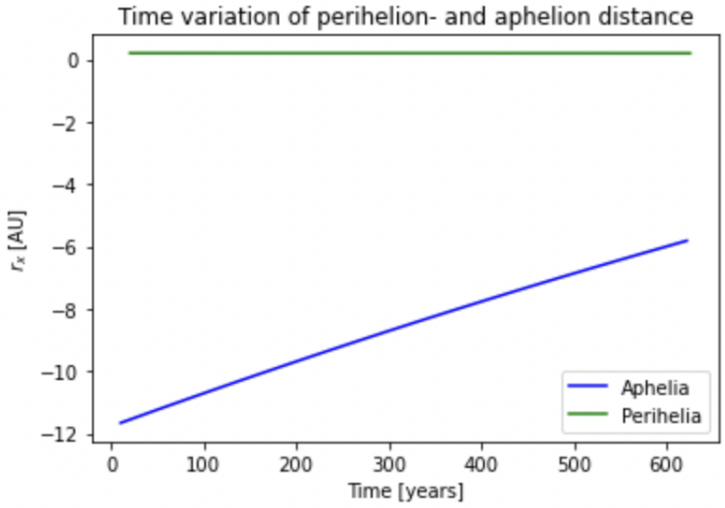

Figure 4.30: Time variation of perihelion- and aphelion distance, for a 65 nm dust grain with an initial perihelion distance 0.2 AU.

The orbital calculations presented in the above figures show that the highly elliptical orbit of a 65 nm dust grain with an initial β-value of 0.49 experiences a significant reduction in aphelion distance as result of mass loss due to sputtering. Although the perihelion distance is reduced as well, this drift is small compared to the aphelion drift, as can be seen in Figure 4.30, confirming that this difference increases with eccentricity.

Again, these orbital calculations only account for the gravitational pull from the Sun and the radiation pressure force, and since the 65 nm dust grain is small, the Lorentz force can be of significance for the dust motion as well. Therefore, as discussed in context of the orbital calculations presented for the 20 nm dust grain in Section 4.4, these results should be regarded as an illustration of the influence of the sputtering mass loss on the dust dynamics. The results indicate that the influence of sputtering is more immediate in the dynamics of dust with higher eccentricities, thus β-values approaching 0.5. This can be explained by the distance dependency of the sputtering mass loss rate. The dust experiences a high mass loss at the perihelion, resulting in a high $\Delta\beta_a$ at the aphelion compared to the previous orbit. Then at the aphelion, the mass loss rate is very low, and so the $\Delta\beta_p$ at the next perihelion is small compared to the previous perihelion as a result. By this reasoning, and as this example of a 65 nm dust grain illustrates, the larger the difference between $\Delta\beta_a$ and $\Delta\beta_p$ is, the more the aphelion distance is reduced.

Even though the influence of sputtering on the dust dynamics is more apparent for elliptical orbits than orbits with lower eccentricities, the average mass loss rate is higher along the orbits that are close to circular in the inner solar system. This is because the dust remains relatively close to the Sun in larger parts of the orbit than it does in the elliptical orbits. This means that the size of the dust is reduced more efficiently in the low β-value orbits, which in turn increases the significance of the Lorentz force (Mann and Czechowski, 2021), and reduces the Poynting-Robertson lifetime (Grün et al., 1985). When considering a more realistic picture of the forces working on nanometer-sized dust in low-eccentricity orbits near the Sun, sputtering may therefore also influence the dynamics of low β-value dust grains, in addition to reducing the mass.

It is worthwhile to consider the presented results in view of the analyses of PSP and SolO observations that were made so far. As described earlier in this work, PSP and SolO observations can be explained with the outward flux of β-meteoroids and an additional component in circular orbits. The calculations made in this work show that the sputtering dust mass loss can produce dust particles in elliptical orbits and that these dust particles have sizes that are close to the detection limit of the PSP and SolO observations.

5

Conclusion

For this thesis, the author did the following calculations. The expressions for sublimation and sputtering mass loss rates provided by Baumann et al. (2020) were used in this work to calculate the mass loss and lifetimes for different dust sizes of different materials, at different distances from the Sun. The sputtering calculations were implemented for both slow solar wind and CME conditions, and the values for the solar wind composition were provided in Killen et al. (2012). For regions outside the sublimation zone, the sputtering lifetimes were compared to the collision lifetimes presented by Grün et al. (1985), in order to determine the size at which the sputtering process is important. From the values for $\beta(m)$ presented by Wilck and Mann (1996), three dust sizes were selected to represent different populations of dust in the inner solar system. One dust grain with radius a of 20 nm which is eventually destroyed when subjected to mass loss, one grain with radius of 200 nm which is ejected from the solar system by the radiation pressure force, and one grain with radius of 2 μm which is eventually ejected when subjected to mass loss. Additionally, a dust grain of 65 nm was chosen to represent dust in highly elliptical orbits around the Sun. A code was written in Python to perform the orbital calculations of these grains, accounting for mass loss, in order to evaluate the influence of mass loss along the trajectories.

Outside the sublimation zone of around 0.1 AU from the Sun, sputtering was found to be the dominant mass loss function for dust grains with radii smaller than 23 μm and 27 μm, for silicate dust at distances of 0.1 AU and 1 AU, respectively, under slow solar wind conditions. The upper size limit for dust of metal oxide and carbon dust was also calculated at these distances, and all materials were evaluated under CME conditions as well. The results were presented in Table 4.2. In general, dust smaller than a few micrometer in the inner solar system is more likely to be destroyed by mass loss due to sputtering than by a collision with another dust grain. The orbits of the selected grain sizes were therefore calculated assuming a mass loss due to sputtering. It was shown that the sputtering process does not affect the trajectory of β-meteoroids significantly. This result supports the assumption that β-meteoroids have constant mass that Szalay et al. (2020) made in their analysis of PSP observations. The possibility of sputtering being a production process of β-meteoroids was investigated by comparing the sputtering ejection time to the Poynting-Robertson lifetime. This it is found unlikely, because the Poynting-Robertson effect causes an inward drift. The calculated dust trajectories show the sputtering causes a drift of both the perihelion- and aphelion distances. As a result, the trajectory covers a ring-shaped area, but for low β-value dust grains the extension of this ring is small.

The possible formation of a ring was also investigated for a particle which β-value high but still below the ejection limit. For a grain with a radius of 65 nm, it was found that the radiation pressure pushes it in a highly elliptical orbit. The aphelion distance was reduced at a high rate because of the sputtering mass loss. This large drift is a result of the high eccentricities of the orbit. This suggest that the influence of mass loss is more immediate on the trajectories of dust with β-values approaching 0.5. Aside from the influences discussed in this thesis, the mass loss due to sputtering can also change the Poynting-Robertson lifetime of the particles, and make the Lorentz force more important. Further investigation of this is suggested as future work.

The observations of dust with PSP and SolO are still continued and data analysis is still ongoing. Zaslavsky et al. (2021) derive that the detected dust particles possibly have radii between 100 and 500 nm, but point out the uncertainties of this estimate. The detection range also depends on the impact speed of the dust, and so the size range is not a fixed boundary. The dust is usually considered to be either in circular orbits or β-meteoroids. Based on the calculations performed in this thesis, there may be a third component of dust present in the regions of the PSP and SolO orbits. The presented calculations of dust grains with radii 65 nm show that grains with β-values just below the ejection limit are significantly affected by sputtering and move in highly elliptical orbits. As opposed to the beta-meteoroids that form an outward going flux, these grains can form an in-going and an outgoing flux. The sizes of these predicted dust grains are

close to the dust size interval observed by PSP and SolO, and it is possible that impacts of such grains can be found in the measurements as well. It is therefore proposed to calculate the flux rates of this dust component in elliptical orbits in detail and to investigate the resulting fluxes of this predicted third dust component onto the satellites.

Bibliography

JR Szalay, P Pokornỳ, SD Bale, ER Christian, K Goetz, K Goodrich, ME Hill, M Kuchner, R Larsen, D Malaspina, et al. The near-sun dust environment: initial observations from parker solar probe. *The Astrophysical Journal Supplement Series*, 246(2):27, 2020.

A Zaslavsky, I Mann, J Soucek, A Czechowski, D Pisa, J Vaverka, N Meyer-Vernet, M Maksimovic, E Lorfèvre, K Issautier, et al. First dust measurements with the solar orbiter radio and plasma wave instrument. *arXiv preprint arXiv:2104.09974*, 2021.

Ingrid Mann, Hiroshi Kimura, Douglas A Biesecker, Bruce T Tsurutani, Eberhard Grün, R Bruce McKibben, Jer-Chyi Liou, Robert M MacQueen, Tadashi Mukai, Madhulika Guhathakurta, et al. Dust near the sun. *Space Science Reviews*, 110(3):269–305, 2004.

NJ Fox, MC Velli, SD Bale, R Decker, A Driesman, RA Howard, Justin C Kasper, J Kinnison, M Kusterer, D Lario, et al. The solar probe plus mission: Humanity's first visit to our star. *Space Science Reviews*, 204(1):7–48, 2016.

Daniel Mueller, Richard George Marsden, OC St Cyr, and Holly Robin Gilbert. Solar orbiter. *Solar Physics*, 285(1):25–70, 2013.

Carsten Baumann, Margaretha Myrvang, and Ingrid Mann. Dust sputtering within the inner heliosphere: a modelling study. In *Annales Geophysicae*, volume 38, pages 919–930. Copernicus GmbH, 2020.

Eberhard Grün, Herbert A Zook, Hugo Fechtig, and RH Giese. Collisional balance of the meteoritic complex. *Icarus*, 62(2):244–272, 1985.

Ingrid Mann, Libor Nouzák, Jakub Vaverka, Tarjei Antonsen, Åshild Fredriksen, Karine Issautier, David Malaspina, Nicole Meyer-Vernet, Jiří Pavl, Zoltan Sternovsky, et al. Dust observations with antenna measurements and its prospects for observations with parker solar probe and solar orbiter. In *Annales Geophysicae*, volume 37, pages 1121–1140. Copernicus GmbH, 2019.

Ch Leinert, I Richter, E Pitz, and B Planck. The zodiacal light from 1.0 to 0.3 au as observed by the helios space probes. *Astronomy and Astrophysics*, 103: 177–188, 1981.

T Mukai and G Schwehm. Interaction of grains with the solar energetic particles. *Astronomy and Astrophysics*, 95:373–382, 1981.

Rainer Behrisch and Wolfgang Eckstein. *Sputtering by particle bombardment: experiments and computer calculations from threshold to MeV energies*, volume 110. Springer Science & Business Media, 2007.

Margaretha Myrvang. Temperature and thermal emission of cosmic dust around the sun, vega and fomalhaut. Master's thesis, UiT Norges arktiske universitet, 2018.

Werner Schmutz, André Fehlmann, Wolfgang Finsterle, Greg Kopp, and Gerard Thuillier. Total solar irradiance measurements with premos/picard. In *AIP conference proceedings*, volume 1531, pages 624–627. American Institute of Physics, 2013.

Ingrid Mann, Andrzej Czechowski, Nicole Meyer-Vernet, Arnaud Zaslavsky, and Hervé Lamy. Dust in the interplanetary medium. *Plasma Physics and Controlled Fusion*, 52(12):124012, 2010.

MS Venzmer and V Bothmer. Solar-wind predictions for the parker solar probe orbit-near-sun extrapolations derived from an empirical solar-wind model based on helios and omni observations. *Astronomy & Astrophysics*, 611:A36, 2018.

RM Killen, DM Hurley, and William M Farrell. The effect on the lunar exosphere of a coronal mass ejection passage. *Journal of Geophysical Research: Planets*, 117(E10), 2012.

I Mann and A Czechowski. Dust observations from parker solar probe: dust ejection from the inner solar system. *Astronomy & Astrophysics*, 650:A29, 2021.

M Wilck and I Mann. Radiation pressure forces on "typical" interplanetary dust grains. *Planetary and Space Science*, 44(5):493–499, 1996.

BR Ragot and SW Kahler. Interactions of dust grains with coronal mass ejections and solar cycle variations of the f-coronal brightness. *The Astrophysical Journal*, 594(2):1049, 2003.

A

Constants used in calculations

Parameter	Value	Comment
m_A (metal oxide)	$4.39 \cdot 10^{-23}$ g	Mean atomic mass of metal oxide dust
m_A (silicate)	$4.08 \cdot 10^{-23}$ g	Mean atomic mass of silicate dust
m_A (carbon)	$1.99 \cdot 10^{-23}$ g	Mean atomic mass of carbon dust
$F_{\odot,0}(r_0 = 1\ \text{AU})$	1361 W m^{-2}	Solar constant (Schmutz et al., 2013)
$n_{p,0}(r_0 = 0.16\ \text{AU})$	214 cm^{-3}	Plasma density (Venzmer and Bothmer, 2018)
$\overline{v}_0(r_0 = 1\ \text{AU})$	20 km s^{-1}	Average impact speed (Grün et al., 1985)
v_{SSW}	300 km s^{-1}	Slow solar wind speed (Baumann et al., 2020)
v_{CME}	500 km s^{-1}	CME wind speed (Baumann et al., 2020)
ρ	2.5 g cm^{-3}	Bulk density of the dust (Mann et al., 2004)
$M_\odot$	$1.9891 \cdot 10^{30}$ kg	Mass of the Sun
G	$6.67408 \cdot 10^{-11}$ m^3 kg^{-1} s^{-2}	Gravitational constant
AU	149597870700 m	Astronomical unit

Table A.1: Overview of the constants used in calculations.

B

Additional results

B.1 Critical size calculations

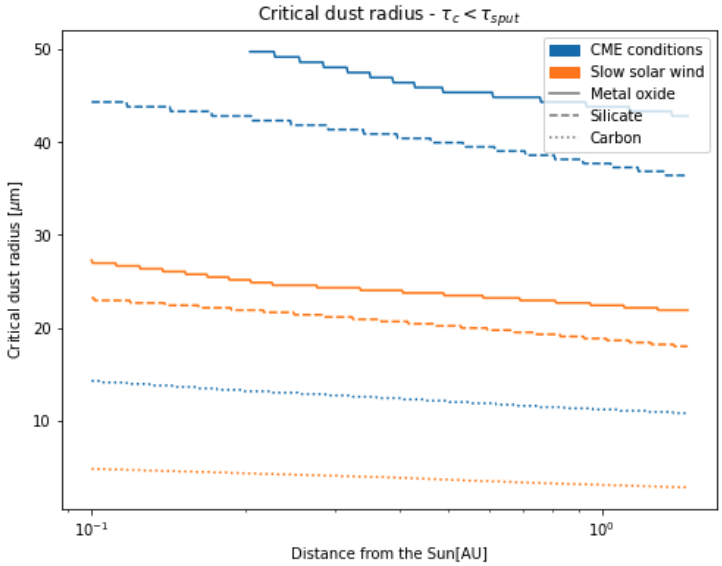

Figure B.1: Critical dust radius, i.e. where the collision lifetime is lower than the sputtering lifetime. Plotted for three dust materials, in both slow solar wind and CME conditions. The steps in the curves are due to the number of data points.

C

Code

This appendix provides the code written by the author to perform the calculations carried out in this thesis, in case it may be helpful to the reader. Section 1 is the code written to calculate the total and relative sputtering yields. Section 2 shows the functions implemented in the code necessary for the orbital calculations. These are discussed in Chapter 3.3 of the text. Finally, the main script for the orbit calculations including mass loss due to sputtering is included in Section 3. Values used in the code are cited if they are found in papers referenced in the text. If they are not cited, they are either user defined, or constants found from references cited in Table A.1.

C.1 Sputtering yield calculations

```
#!/usr/bin/env python
# coding: utf-8

# In[1]:


## Import libraries
import numpy as np
from math import *
from operator import add


# In[2]:


## DATA

# Parameters explained:
#    - k: Solar wind ion type,  k_label: [all the solar wind
                                 ions]
#    - i: Dust species,         i_label: [all the types of dust]
#    - j: Sputtered atom,       j_species: [all the atom types
                                 in that species]
#    - w: Wind conditions,      w_label: [two solar wind
                                 conditions]

# Output of this section
#    - c_k_w:   Solar wind composition for [CME, sSW]
#    - Y_kjiw:  Specific sputtering yield for:
#                 - a given solar wind ion type
#                 - on a given dust atom type
#                 - in a given dust species type
#                 - under a given solar wind condition


# Labels
k_label         = ['H', 'He', 'C', 'O', 'N', 'Fe', 'Ne', 'Mg', '
                                Si', 'S']
i_label         = ['Metal oxide', 'Silicate', 'Carbon']
w_label         = ['CME', 'Slow solar wind']
j_metaloxide    = ['Fe', 'Mg', 'O']
j_silicate      = ['Mg', 'Fe', 'Si', 'O']
j_carbon        = ['C']
j_label         = [j_metaloxide, j_silicate, j_carbon]



## ---- Solar wind composition: Data from Killen et al. (2012)
                                - Table 6

# Ion compositions in the CME solar wind and slow solar wind.
                                Numbers are percentages.
```

```
c_k_CME = [0.670037, 0.30, 3.67e-3, 9.66e-3, 7.73e-4,
           7.05e-3, 3.09e-3, 2.80e-3, 1.74e-3, 1.18e-3]
c_k_sSW = [0.9588979, 0.04, 3.19e-4, 4.86e-4, 4.19e-5,
           5.05e-5, 4.95e-5, 6.81e-5, 6.28e-5, 2.43e-5]

# Combine solar wind conditions
c_k_w = [c_k_CME, c_k_sSW]

## ---- Sputtering yields: Data from Baumann et al. (2020)
                                  supplemented material

# CME Conditions
# Metal oxide dust: Mg_0.4 Fe_0.6 O
Y_jFe = [0.0077, 0.0533, 0.2482, 0.3546, 0.2949, 0.9612, 0.4438
                                  , 0.5240, 0.5878, 0.6482]
Y_jMg = [0.0261, 0.1498, 0.6800, 0.9845, 0.8078, 2.6600, 1.2100
                                  , 1.4400, 1.6000, 1.8700]
Y_jO  = [0.0353, 0.1910, 0.9350, 1.3200, 1.1000, 3.6000, 1.6600
                                  , 1.9400, 2.1600, 2.4300]
Y_kj_metaloxide_CME = [Y_jFe, Y_jMg, Y_jO]

# Silicate dust
Y_jMg = [0.0103, 0.0540, 0.2663, 0.3605, 0.3209, 0.9751, 0.4367
                                  , 0.5222, 0.5772, 0.6676]
Y_jFe = [0.0049, 0.0281, 0.1440, 0.2008, 0.1748, 0.5217, 0.2343
                                  , 0.2875, 0.3054, 0.3534]
Y_jSi = [0.0039, 0.0254, 0.1341, 0.1814, 0.1613, 0.4816, 0.2133
                                  , 0.2575, 0.2834, 0.3217]
Y_jO  = [0.0305, 0.1696, 0.8738, 1.1800, 1.0400, 3.1700, 1.4100
                                  , 1.7100, 1.8700, 2.1300]
Y_kj_silicate_CME = [Y_jMg, Y_jFe, Y_jSi, Y_jO]

# Carbon dust
Y_jC = [0.0055, 0.0365, 0.1706, 0.2689, 0.1902, 1.3500, 0.4267,
                                   0.6000, 0.7200, 0.8300]
Y_kj_carbon_CME = [Y_jC]


# Slow solar wind conditions
# Metal oxide dust: Mg_0.4 Fe_0.6 O
Y_jFe = [0.0083, 0.0621, 0.2878, 0.3812, 0.3505, 0.9622, 0.4828
                                  , 0.5667, 0.6210, 0.6807]
Y_jMg = [0.0288, 0.1663, 0.7942, 1.0600, 0.9414, 2.6800, 1.3400
                                  , 1.5700, 1.7300, 1.9100]
Y_jO  = [0.0379, 0.2293, 1.0600, 1.4400, 1.2700, 3.6600, 1.8000
                                  , 2.1200, 2.3400, 2.5900]
Y_kj_metaloxide_sSW = [Y_jFe, Y_jMg, Y_jO]

# Silicate dust
Y_jMg = [0.0109, 0.0643, 0.3014, 0.4103, 0.3614, 0.9772, 0.4925
                                  , 0.5636, 0.6416, 0.7136]
Y_jFe = [0.0047, 0.0354, 0.1603, 0.2171, 0.1924, 0.5234, 0.2704
                                  , 0.3010, 0.3502, 0.3899]
```

```
Y_jSi = [0.0040, 0.0334, 0.1469, 0.1974, 0.1759, 0.4762, 0.2458
                                 , 0.2769, 0.3141, 0.3431]
Y_jO  = [0.0346, 0.2199, 0.9641, 1.3400, 1.1600, 3.1800, 1.6000
                                 , 1.8200, 2.0900, 2.3100]
Y_kj_silicate_sSW = [Y_jMg, Y_jFe, Y_jSi, Y_jO]

# Carbon dust
Y_jC = [0.0076, 0.0567, 0.2389, 0.3614, 0.2606, 1.3500, 0.4620,
                                  0.6000, 0.7200, 0.8300]
Y_kj_carbon_sSW = [Y_jC]


# ------------------------------------------------------
# Combine species for seperate solar wind conditions
Y_kji_CME = [Y_kj_metaloxide_CME, Y_kj_silicate_CME,
                                 Y_kj_carbon_CME]
Y_kji_sSW = [Y_kj_metaloxide_sSW, Y_kj_silicate_sSW,
                                 Y_kj_carbon_sSW]

# Combine solar wind conditions
Y_kjiw = [Y_kji_CME, Y_kji_sSW]


# In[5]:


## Main - calculate the relative and total sputtering yields

# Dictionary with data and for storage of calculated yields
wind_dict = {w_label[0]:   {'c_k':    c_k_w[0],
                            'Y_kji':  Y_kjiw[0],
                            'Y_k':    [],
                            'Y_tot':  [],
                            'Y_rel':  []  },

             w_label[1]:   {'c_k':    c_k_w[1],
                            'Y_kji':  Y_kjiw[1],
                            'Y_k':    [],
                            'Y_tot':  [],
                            'Y_rel':  [] }
                }


 # For all wind conditions
for w in range(0, len(w_label)):

    # For all dust materials, i
    for i in range(0, len(i_label)):

        Y_k = []

        # For all solar wind ions, k
        for k in range(0, len(k_label)):
```

```
            Y_sum = 0

            # For all dust components, j
            for j in range(0, len(j_label[i])):

                Y_j = wind_dict[w_label[w]]['Y_kji'][i][j][k]
                Y_sum += Y_j

            Y_k.append(wind_dict[w_label[w]]['c_k'][k]*Y_sum)


        # Calculate total yield
        Y_tot = sum(Y_k)

        # Calculate relative yield of each SW ion, k
        Y_rel = [n/Y_tot for n in Y_k]

        # Store
        wind_dict[w_label[w]]['Y_k'].append(Y_k)
        wind_dict[w_label[w]]['Y_tot'].append(Y_tot)
        wind_dict[w_label[w]]['Y_rel'].append(Y_rel)


# In[ ]:
```

C.2 Functions

```
#!/usr/bin/env python
# coding: utf-8

# In[1]:


## Import libraries
import numpy as np
from math import *
from scipy.interpolate import interp1d
from operator import add


# In[2]:


## Parameters explained

# k: Solar wind ion type
# i: Dust species
# j: Dust component type
# w: Solar wind condition

# Defining strings:
```

```
#     - i = 'metaloxide', 'silicate' or 'carbon'
#     - w = 'CME' or 'Slow solar wind'


# In[3]:


## Defining functions

# ------ General functions ------

def Mass_to_Radius(rho, m_dust):
    r_dust = np.cbrt(3*m_dust/(4*np.pi*rho))  #[m]
    return(r_dust)

def Radius_to_Mass(rho, r_dust):
    m_dust = (rho*4*np.pi*(r_dust**3)/3)      #[g]
    return(m_dust)



# ------ Functions for sputtering ------

def MaterialProperties(i):

    if i == 0:
        i = 'metaloxide'
    elif i == 1:
        i = 'silicate'
    else:
        i = 'carbon'

    # Constants
    u = 1.66e-24  # [g], atomic mass unit

    # Molar masses of atoms [u] (g/mol)
    M_Mg, M_Si, M_O, M_Fe, M_C = 24.305, 28.0855, 15.999, 55.
                                    845, 12.011


    # Metal oxide
    if i == 'metaloxide':

        # Mass of one dust molecule [u]
        M_metaloxide = 0.4*M_Fe + 0.6*M_Mg + M_O

        # Mean mass of the sputtered atoms [g]
        m_A = (M_metaloxide/2)*u

        # Mean molecular mass of the sublimated material [g]
        M   = (M_metaloxide/1)*u

    # Silicate dust
    if i == 'silicate':
        M_silicate = M_Mg + M_Fe + M_Si + (4*M_O)    # [u]
```

```
        m_A = (M_silicate/7)*u                          # [g]
        M   = (M_silicate/1)*u                          # [g]

    # Carbon dust
    if i == 'carbon':
        M_carbon = M_C                  # [u]
        m_A = (M_carbon/1)*u            # [g]
        M   = (M_carbon/1)*u            # [g]

    return(m_A, M)


def PlasmaDensity(r):

    AU = 149597870700      # Astronomical unit [m]
    r_mag = np.sqrt(r[0]**2 + r[1]**2)          # [m]

    # Reference value from Venzmer and Bothmer (2018):
    n0 = 214e6                                  # [/m3]
    r0 = 0.16*AU                                # [m]

    n = (n0*r0**2)/r_mag**(2)                   # [/m3]

    return(n)

def SolarWindFlux(r, w):

    # Solar wind speed [m/s], Baumann et al. (2020)
    if w == 0:
        v_p = 500e3
    elif w == 1:
        v_p = 300e3

    # Plasma density [/m3]
    n_p = PlasmaDensity(r)

    # Solar wind flux
    f_SW = v_p*n_p

    return(f_SW)


def SputteringYield(w, i):

    Y_tot_CME = [0.2842414438, 0.2019958852, 0.
                                    03275410709999999]
    Y_tot_sSW = [0.09367470409000003, 0.06862100380999998, 0.
                                    01001568168]
    Y_tot = [Y_tot_CME, Y_tot_sSW]

    return(Y_tot[w][i])


def MassLossSputtering(r_dust, r, w, i):
```

```
    # Total sputtering yield
    Y_tot = SputteringYield(w, i)

    # Solar wind flux
    f_SW = SolarWindFlux(r, w)  # [/m3]

    # Mean mass of the sputtered atoms
    m_A, M = MaterialProperties(i)

    # Area of the grain - Sputtering cross section
    A = np.pi*(r_dust**2)       # [m2]

    # Mass loss rate
    m_dot = -f_SW*Y_tot*A*m_A   # [g/s]

    return(m_dot)



# ------- Functions for orbital calculations --------

def GetMass(m, r, rho, t, dt, r_dust, w, i):

    # Constants
    AMU      = 1.66e-24         # Atomic mass number [g]
    m_olivin = 238.296*AMU      # Mass of Olivin [g]

    # Get the current mass loss rate
    m_dot = MassLossSputtering(r_dust, r, w, i)  # [g/s]

    # New mass
    m = m + m_dot*dt                             # [g]

    m_A, M = MaterialProperties(i)

    # Evaluate whether lower mass limit is reached
    if m < m_olivin:
        destruction = 1
        print('Dust is destroyed at time {} s'.format(t))
    else:
        destruction = 0

    return(m, destruction)


def GetBeta(m):

    m = np.log(m)

    ## --- Wilck et al. 1996: Relation between beta and mass
                                  for astroidal dust.
    m_A    = [1.4e-17, 4.4e-16, 1.4e-14, 4.4e-13, 1.4e-11, 4.4e
                                  -10, 1.4e-8, 4.4e-7]
```

```
    beta_A = [0.106, 0.163, 0.751, 0.772, 0.222, 0.061, 0.018,
                                    0.005]

    ## --- Interpolate above data to get functions f(m) = beta
    f_A = interp1d(np.log(m_A), beta_A, kind='quadratic')

    # Get beta(m)
    if m <= np.log(m_A[-1]) and m >= np.log(m_A[0]): # Within
                                    interp range
        beta = f_A(m)
    elif m < np.log(m_A[0]):   # Below interp range
        beta = f_A(np.log(m_A[0]))
    elif m > np.log(m_A[-1]):  # Above interp range
        beta = f_A(np.log(m_A[-1]))

    return(beta)


# Newtonian method
def GetAcceleration(beta, m, phi, r):

    # Constants
    M_sun     = 1.9891e30    # Solar mass [kg]
    G         = 6.67408e-11 # Gravitational constant [m3 kg-1 s-
                                    2]
    mu        = M_sun*G      # Gravitational standard unit

    r_mag = np.sqrt(r[0]**2 + r[1]**2)

    # Solve equation of motion
    Fg_red =(mu/(r_mag**2))*(beta-1)
    a = [Fg_red*np.cos(phi), Fg_red*np.sin(phi)]

    return(a)




def EulerCromer(m, beta, r, v, phi, dt):

    # Get current acceleration
    a = GetAcceleration(beta, m, phi, r)

    # Calculate next velocity and position
    v_next = list(map(add, v, [n*dt for n in a]))
    r_next = list(map(add, r, [n*dt for n in v_next]))

    # Calculate next phi
    r_next_mag = np.sqrt((r_next[0]**2) + (r_next[1]**2))
    phi_i = np.arccos(r_next[0]/r_next_mag)

    # Trigonometric evaluation of quadrants
    if r_next[0] > 0 and r_next[1] > 0:
        phi_next = phi_i
```

```
    elif r_next[0] < 0 and r_next[1] > 0:
        phi_next = phi_i
    elif r_next[0] < 0 and r_next[1] < 0:
        phi_next =  2*np.pi - phi_i
    else:
        phi_next = 2*np.pi - phi_i

    return(r_next, v_next, phi_next)

def Leapfrog(t, r, v, phi, dt, beta, v0_circ):

    # Current acceleration
    a = GetAcceleration(beta, m, phi, r)

    # First iteration, have to hardcode x1
    if t == 0:
        v_next = list(map(add, [v0_circ*np.sin(phi0), v0_circ*
                                np.cos(phi0)], [n*(0.5*
                                dt) for n in a]))
        r_next = list(map(add, r, [n*dt for n in v_next]))
    else:
        v_next = list(map(add, v, [n*dt for n in a]))
        r_next = list(map(add, r, [n*dt for n in v_next]))

    # Calculate next angle
    r_next_mag = np.sqrt((r_next[0]**2) + (r_next[1]**2))
    phi_i = np.arccos(r_next[0]/r_next_mag)

    if r_next[0] > 0 and r_next[1] > 0:
        phi_next = phi_i
    elif r_next[0] < 0 and r_next[1] > 0:
        phi_next = phi_i
    elif r_next[0] < 0 and r_next[1] < 0:
        phi_next =  2*np.pi - phi_i
    else:
        phi_next = 2*np.pi - phi_i


    return(r_next, v_next, phi_next)


# ------- Function for the collision lifetimes -------

def LifetimeCollision(r, r_dust, rho):

    ## Data read from Grun et al. (1985) Fig. 6 in pixels. r =
                                    1 AU
    x_m = [10, 30, 50, 70, 80, 90, 100, 110, 115, 120, 125, 130
                                    , 135, 140, 150, 160, 170,
       180, 190, 200, 210, 220, 230, 240, 250, 260, 265, 270,
                                      275, 280, 290, 300, 310,
       320, 330, 340, 350, 360, 370, 380, 390, 400, 410, 420,
                                      430, 440, 450, 460, 470,
       480, 490, 500, 510]
```

```
    x_T = [33, 35, 38, 42, 45, 52, 58, 67, 74, 73, 74, 73, 72,
                                    70, 68, 66, 64, 62, 61, 59,
                                     59, 58, 57, 59,
       62, 64, 67, 70, 73, 75, 84, 92, 102, 111, 119, 128, 137,
                                         145, 152, 158, 163, 166
                                        , 167, 167, 165,
       161, 157, 152, 145, 137, 130, 122, 115]

    ## Convert from pixel to logartihmix exponentials
    # (Equations derived from screen properties)
    y_m = []
    y_T = []
    for i in range(0, len(x_m)):
        y_m.append(np.power(10, ((x_m[i]-10)/25)-18))    # [g]
        y_T.append(np.power(10, (-(x_T[i]-10)/48)+7))    # [
                                         years]

    ## Make the reference array
    Tau_c_ref = [y_m, y_T]

    # Constants
    AU = 149597870700         # Astronomical unit [m]
    r0 = 1*AU                 # Reference distance

    # Calculate Tau_c at current r for all masses first
    T_c = []
    for i in range(0, len(Tau_c_ref[1])):
        T_c.append(Tau_c_ref[1][i]*(r/r0)**1.8)

    # Return a value for the current dust mass at the current
                                       distance
    f_Tau = interp1d(Tau_c_ref[0], T_c)
    t_coll = f_Tau(Radius_to_Mass(rho, r_dust))  # [years]

    return(t_coll)
```

C.3 Orbital calculations

```
#!/usr/bin/env python
# coding: utf-8

# In[2]:


## Import libraries
import numpy as np
from math import *
import matplotlib.pyplot as plt
from scipy.interpolate import interp1d
from operator import add


# In[3]:


## Define constants and user defined parameters

# --- Constants
M_sun = 1.9891e30      # Solar mass [kg]
G     = 6.67408e-11    # Gravitational constant [m3/kg/s2]
mu    = M_sun*G        # Gravitational standard unit [m3/s2]
AU    = 149597870700   # Astronomical unit [m]
rho   = 2.5e6          # Bulk density of the dust [g/m3]

# --- User defined inital parameters
r_dust = 200e-9                      # Initial dust radius [m]
m0   = (rho*4*np.pi*(r_dust**3)/3)   # Initial mass [g]
r0   = 0.1*AU                        # Source region [m]
v0   = np.sqrt(mu/r0)                # Initial velocity [m/s]
T    = 2*np.pi*np.sqrt((r0**3)/mu)   # Initial orbital period [s]
phi0 = 0                          # Initial true anomaly [rad]

# --- Iterative code parameters
t0     = 0                       # Inital time [s]
dt     = 1000                    # Step size [s]
t_end  = 7000*T                  # Run the code for this long [s]

# --- Define dust/condition parameters
i = 1                            # Silicate dust

w_label = ['CME', 'Slow solar wind']
i_label = ['Metal oxide', 'Silicate', 'Carbon']


# In[13]:



# ------- Orbit calculations --------
```

```
# Create empty dictionary for storage
wind_main = {w_label[0]: {},
             w_label[1]: {}
                }

# For all solar wind conditions
for w in range (0, len(w_label)):

    # Set initial conditions
    phi, m, t = phi0, m0, t0
    beta = GetBeta(m)
    r = [r0*np.cos(phi), r0*np.sin(phi)]
    v = [v0*np.sin(phi), v0*np.cos(phi)]

    # Create storage space
    main_dict = {'pos_x': [r[0]],
                 'pos_y': [r[1]],
                 'vel_x': [v[0]],
                 'vel_y': [v[1]],
                 'phi': [phi],
                 'mass': [m],
                 'beta': [beta],
                 'time': [t],
                 'lifetime': 0   # Overwrite if dust is
                                                 destroyed
    }

    # Calcualte orbit
    destruction = 0
    while t < t_end and destruction == 0:

        # Get current mass
        m, destruction = GetMass(m, r, rho, t, dt, r_dust, w, i
                                         )

        # Get corresponding beta
        beta = GetBeta(m)

        # Get next ephemerals
        r_next, v_next, phi_next = Leapfrog(t, r, v, phi, dt,
                                        beta, v0)

        # Increment time
        t += dt

        # Store parameters
        main_dict['pos_x'].append(r_next[0])
        main_dict['pos_y'].append(r_next[1])
        main_dict['vel_x'].append(v_next[0])
        main_dict['vel_y'].append(v_next[1])
        main_dict['phi'].append(phi_next)
        main_dict['mass'].append(m)
        main_dict['beta'].append(beta)
        main_dict['time'].append(t)
```

```
        if destruction == 1:
            main_dict['lifetime'] = main_dict['time'][-2]

        r, v, phi = r_next, v_next, phi_next

    # Store results in wind_main dictionary
    wind_main[w_label[w]] = main_dict
```